

Quarterly Report for
Contract DE-FG36-08GO18192
Stanford Geothermal Program
January-March 2011

Table of Contents

1. FRACTURE CHARACTERIZATION USING PRODUCTION DATA	3
1.1 SUMMARY	3
1.2 INTRODUCTION	3
1.3 THE SOULTZ FLOW MODEL	4
1.4 TRACER RETURNS AT VARIOUS FLOW CONFIGURATIONS	9
1.5 OPTIMIZATION OF INJECTION SCHEDULING	15
1.6 FUTURE WORK	23
2. FRACTURE CHARACTERIZATION OF ENHANCED GEOTHERMAL SYSTEMS USING NANOPARTICLES	25
2.1 SUMMARY	25
2.2 INTRODUCTION	26
2.3 EXPERIMENTAL SETUP AND CHARACTERIZATION OF FRACTURED GREYWACKE	27
2.4 FLUORESCENT SILICA MICROSPHERES: CHARACTERIZATION AND INJECTION EXPERIMENT	30
2.5 RESULTS	41
2.6 SYNTHESIS AND CHARACTERIZATION OF TIN-BISMUTH NANOPARTICLES	44
2.7 FUTURE WORK	47
3. FRACTURE CHARACTERIZATION USING RESISTIVITY	49
3.1 SUMMARY	49
3.2 INTRODUCTION	49
3.3 RESISTIVITY MODEL	51
3.4 TIME HISTORY OF POTENTIAL DIFFERENCE	53
3.5 WATER FLOW ANALOGY OF ELECTRICAL FLOW	56
3.6 FUTURE WORK	59
4. FRACTURE APERTURE DETERMINATION USING THERMAL AND TRACER DATA	61

4.1 SUMMARY	61
4.2 INTRODUCTION	61
4.3 METHODOLOGY	62
4.4 PRELIMINARY CALCULATIONS AND RESULTS	63
4.5 REVIEW OF RELATED LITERATURE	64
4.6 FUTURE WORK	65
5. REFERENCES	69

1. FRACTURE CHARACTERIZATION USING PRODUCTION DATA

This research project is being conducted by Research Assistant Egill Juliusson, Senior Research Engineer Kewen Li and Professor Roland Horne. The objective is to investigate ways to characterize fractured geothermal reservoirs using production data.

1.1 SUMMARY

Our investigation continues to examine the extent to which tracer transport varies as a function of injection rate in fractured reservoirs. Additionally, a method for using tracer data to optimize reinjection schedules has been developed.

It is important to understand how tracer returns vary as a function of the injection and production rates in a given field, especially in enhanced geothermal systems where one would not expect large groundwater flow currents. Understanding of this variation helps prevent misinterpretation of tracer data and paves the way for utilization of tracers to determine effective injection strategies. Effective injection strategies for geothermal systems might aim towards maximizing the heat extracted from the reservoir, or maximizing the net present value of extracting energy from the resource over a given time period.

This discussion describes the development of a reservoir model based on various data sources obtained from the Soultz enhanced geothermal reservoir. The layout of the main flow paths was based on seismic imaging, and a few additional flow paths were added stochastically. Flow simulations were performed with a two-dimensional discrete fracture model. These simulations were used to calibrate the properties of the main flow paths to measurements of tracer returns.

The calibrated discrete fracture flow model was used to simulate tracer tests as seven different injection rate configurations. The tracer returns were then compared for each injector-producer well pair. The results showed that these returns varied significantly as a function of the flow rate configuration. This variability could be reduced significantly by obtaining the effective flow rate connectivity and using that to determine the tracer kernels (as discussed in the quarterly reports of Summer and Fall 2010).

Lastly, three methods for injection rate optimization are presented. These methods were tested with a simple reservoir model with two injectors and two producers. The estimated flow rates, tracer responses and thermal breakthrough were used to develop objective functions that compute: a) the mass produced; b) the energy extracted; c) the net present value of production, over a given period. A nonlinear optimization algorithm was used to find the injection rates that would minimize (or maximize) the given objective function. The results for this simple test case seem intuitive and promising. Ways to verify the effectiveness of the method are still under investigation. A test on the more complex Soultz flow model is planned.

1.2 INTRODUCTION

Understanding interwell connectivity is a requirement for geothermal field management. For example, premature thermal breakthrough can be prevented if an injector-producer pair

is known to be well connected. A quantitative way of defining the connectivity leads to the possibility of optimizing reinjection scheduling (Lovekin and Horne, 1989).

Julusson and Horne (2010) discussed a quantitative way of determining injector-producer connectivity from tracer tests. The connectivity was defined in terms of a convolution kernel representative of the flow paths connecting each injector-producer pair. A method for estimating these kernels was developed, under steady-state flow conditions. The observation was made that the kernels do not apply for all flow rate conditions and were therefore of limited use for reinjection scheduling.

A way to account for the variability in flow rates was discussed by Juliusson and Horne (2011). The key addition was that the convolution kernels were represented in terms of cumulative flow, and could therefore be applied at variable flow rate conditions. The mathematical basis for the method depended on the one-dimensional advection-dispersion equation. The method works remarkably well for flow through naturally fractured reservoirs because the bulk of the streamlines go along the few largest fractures in the reservoir.

The variability of tracer returns as a function of flow rate was tested further in current quarter by developing a flow model with data from the Soultz enhanced geothermal system. Tracer simulations on the model show that the tracer kernel method works well for those injector-producer pairs which are strongly connected.

Finally, a few different options for using tracer data to optimize reinjection schedule are introduced and tested with a simple model of two injectors and two producers.

1.3 THE SOULTZ FLOW MODEL

In this section we describe the development of a flow model rooted in data obtained from the Soultz-sous-Forêts enhanced geothermal system in France. The Soultz reservoir was chosen because it has been investigated extensively and observations have been reported in dozens of publications.

Some of the more recent interpretations of seismic data were provided to us by Place et al. (2011). These data were imported into the discrete fracture software FRACMAN. Seven of these fractures are shown in Figure 1.1.

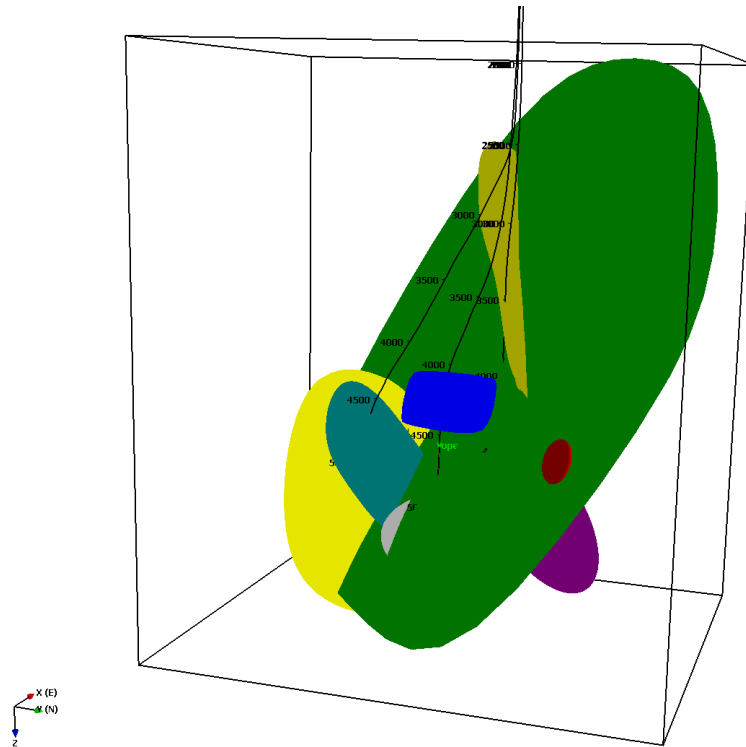


Figure 1.1: Seven of the fractures (or faults) found in the Soultz reservoir by Place et al. (2011).

Additional fractures were created based on statistical correlations reported by Massart et al. (2010). The additional fractures were created in four sets. The sets have a mean North-South direction with East and West dips, forming conjugate sets. First a few relatively large East and West dipping fractures were created at random locations in the region of interest. Then 500 additional fractures of smaller size were generated in clusters around the preexisting fractures. One such stochastic fracture set is shown in Figure 1.2. Note that the Fisher dispersion recorded for the trend and dip was quite low, indicating that the fracture orientations varied a great deal.

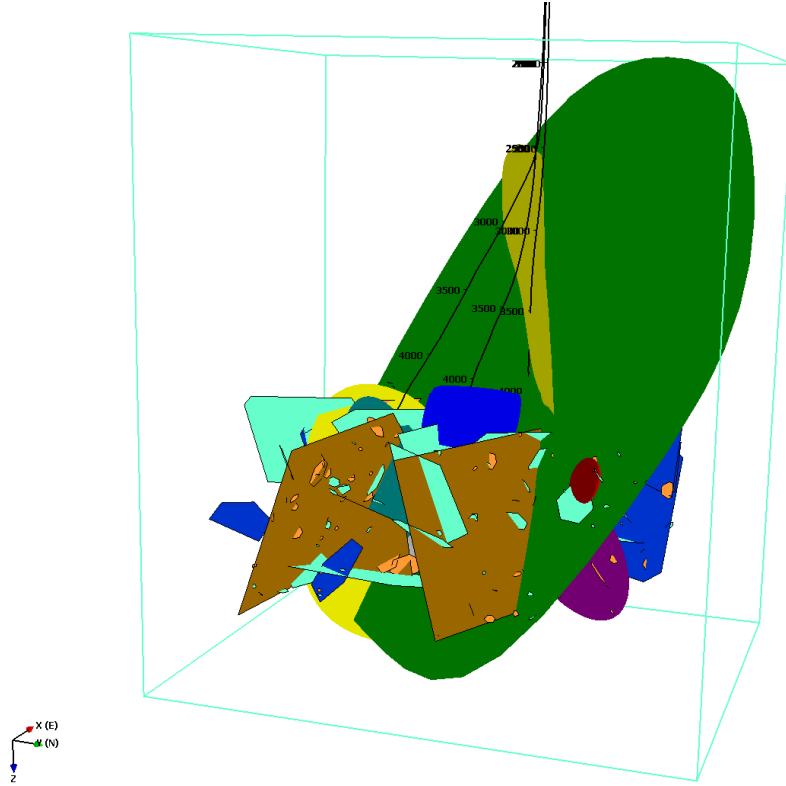


Figure 1.2: A number of stochastically generated fractures were added to the model. The spatial distribution of the fractures was based on the findings of Massart et al. (2010).

Moving from fracture generation to three-dimensional flow simulations proved challenging. We needed to create a model capable of handling pressure, solute and thermal transport. FRACMAN was not capable of handling such simulations properly. To be able to capture the effects of the high permeability fractures, we wanted to use discrete fracture simulations, but creating three-dimensional grids for such models and finding a simulator that can work with those grids seemed to be overly complicated at this point. Therefore we decided to start by assuming that the fractures were all vertical. This allowed the grid to be generated by the Triangle mesh generator (with the grid conforming to the main fractures) and simulations were run using FEFLOW. The fractures were represented by discrete fracture elements.

Massart et al. (2010) suggested the following correlations between fracture size and aperture:

$$L = k_1 b^{D_1} \quad (0.1)$$

where L is the effective fracture radius and b is the fracture aperture. The parameter D_1 is the fractal dimension which Massart determined to be 1.04 and k_1 is a correlation parameter which is relatively hard to quantify (Massart suggested $k_1=400$). A similar

correlation was assumed to exist between the hydraulic conductivity of the fractures and the fracture aperture:

$$K = \left(\frac{b}{k_2} \right)^{D_2} \quad (0.2)$$

where K is the hydraulic conductivity and k_2 and D_2 are undetermined parameters. The reservoir thickness was assumed to be 500 m and that the height of each of the fractures was taken to be the minimum of the fracture length and 500 m. The porosity of the fractures was assumed to be 4%. The matrix porosity and permeability were much smaller than the corresponding fracture properties and therefore the matrix had negligible effect on the solute transport. A dispersion coefficient of 50 m was used for the longitudinal direction and 5 m for the transverse flow direction.

Gentier et al. (2010) reported the results of a tracer test carried out in Soultz in 2005. Tracer was injected into well GPK3 (fluid injection rate $15 \times 10^{-3} \text{ m}^3/\text{s}$) and produced from wells GPK2 (fluid production rate $12 \times 10^{-3} \text{ m}^3/\text{s}$) and GPK4 (fluid production rate $3 \times 10^{-3} \text{ m}^3/\text{s}$). No pumps were used for the production and therefore the wells in the simulation were designed to produce at a constant bottomhole pressure. We attempted to tune the fracture lengths and connections, and the parameters k_1 , k_2 , and D_2 , until the model results gave an approximate match to the measured data. The history match shown in Figure 1.3 was obtained from the flow model illustrated in Figure 1.4 with $k_1=1000$, $k_2=50$, and $D_2=1.8$. The history match could probably have been improved by adding a larger secondary flow path between GPK2 and GPK3. However, we let this match suffice as the main goal was to create a reservoir model with somewhat realistic dimensions and parameter distributions. This seemed to be accomplished with the current model.

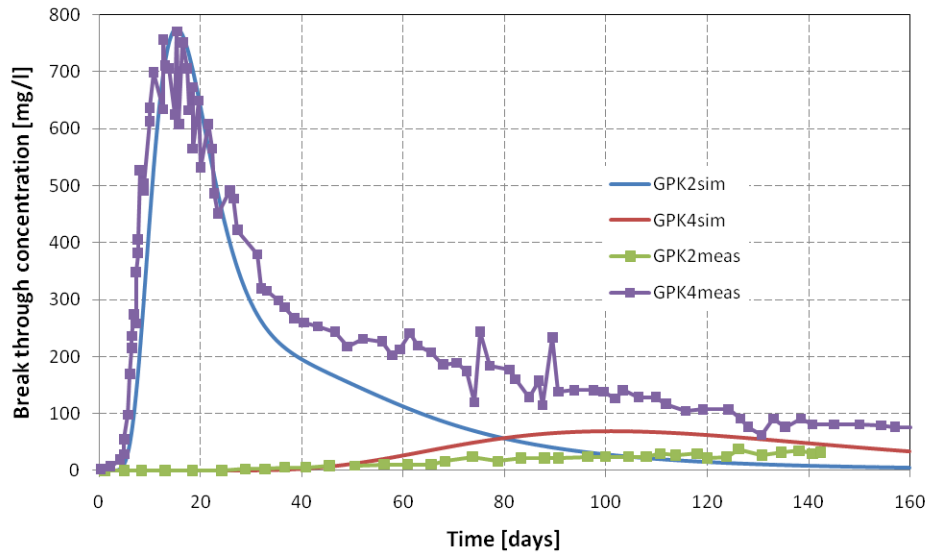


Figure 1.3: Match between simulated and measured breakthrough concentration for the tracer test performed in the Soultz reservoir.

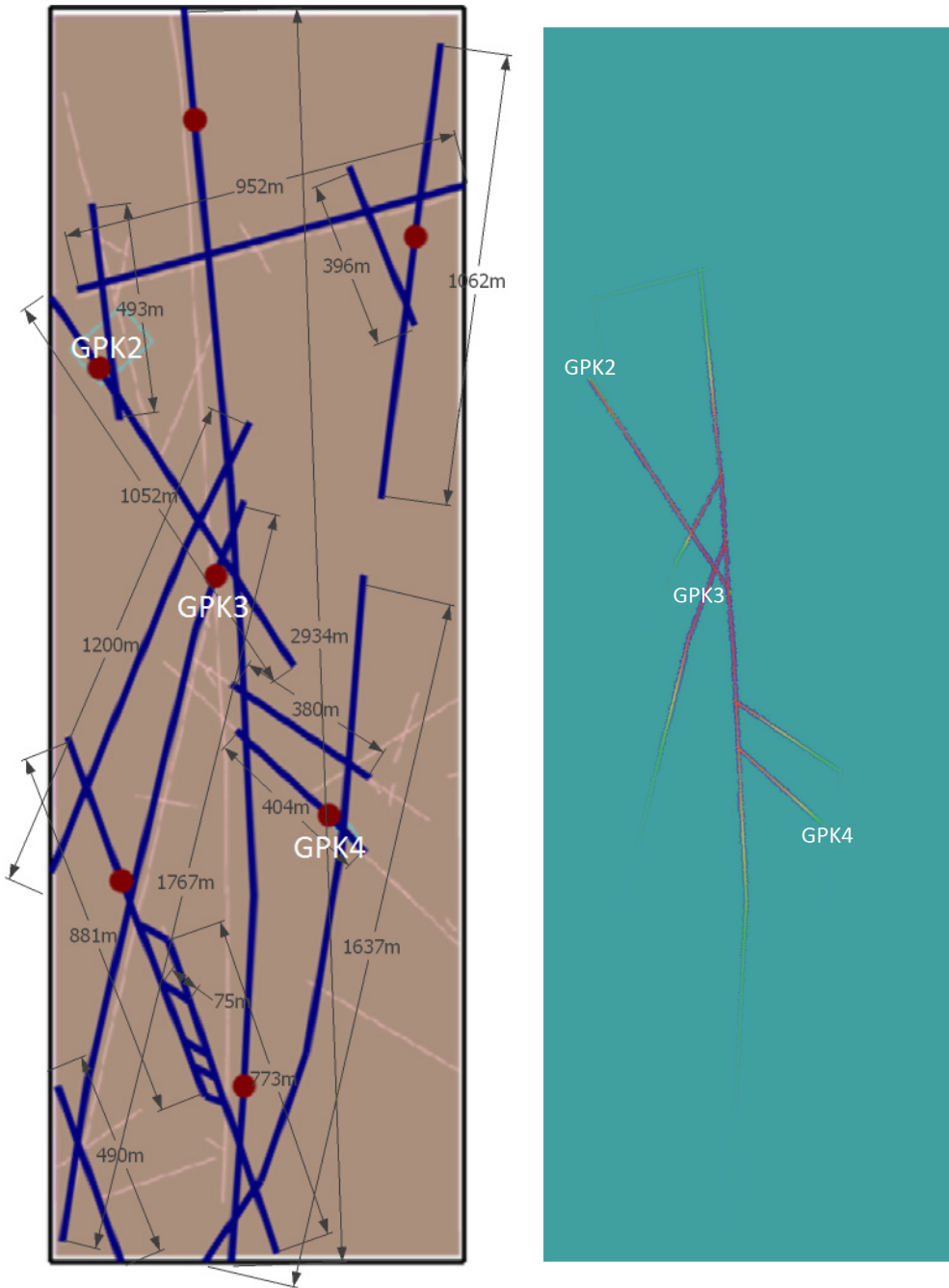


Figure 1.4: The left part of this figure shows the layout and approximate lengths of the fractures used in the Soutz model. The right part shows the tracer distribution in the reservoir at the end of the 160 day tracer test simulation. The existing wells are labeled GPK2, GPK3 and GPK4. The additional red dots in the left part of the figure represent four wells that were added to the model for further testing.

1.4 TRACER RETURNS AT VARIOUS FLOW CONFIGURATIONS

The two-dimensional Soutz flow model was used to investigate the expected variability in tracer returns under various injection rate configurations. Four additional wells were added to the model, such that there were four designated injection wells and three production wells (Figure 1.5).

Table 1.1 lists the simulation runs which involved seven different injection rate configurations. A continuous concentration of tracer was injected into each of the injectors, one at a time. This resulted in a total of 28 simulation runs.

Table 1.1: List of simulations run with various injection rate configurations and tracer allocations.

	Run #	I1 [m3/d]	I2 [m3/d]	I3 [m3/d]	I4 [m3/d]	I1 [mg/l]	I2 [mg/l]	I3 [mg/l]	I4 [mg/l]
Config. 1	1	1200	1200	4800	4800	1	0	0	0
	2	1200	1200	4800	4800	0	1	0	0
	3	1200	1200	4800	4800	0	0	1	0
	4	1200	1200	4800	4800	0	0	0	1
Config. 2	5	1200	4800	1200	4800	1	0	0	0
	6	1200	4800	1200	4800	0	1	0	0
	7	1200	4800	1200	4800	0	0	1	0
	8	1200	4800	1200	4800	0	0	0	1
Config. 3	9	1200	4800	4800	1200	1	0	0	0
	10	1200	4800	4800	1200	0	1	0	0
	11	1200	4800	4800	1200	0	0	1	0
	12	1200	4800	4800	1200	0	0	0	1
Config. 4	13	4800	1200	1200	4800	1	0	0	0
	14	4800	1200	1200	4800	0	1	0	0
	15	4800	1200	1200	4800	0	0	1	0
	16	4800	1200	1200	4800	0	0	0	1
Config. 5	17	4800	4800	1200	1200	1	0	0	0
	18	4800	4800	1200	1200	0	1	0	0
	19	4800	4800	1200	1200	0	0	1	0
	20	4800	4800	1200	1200	0	0	0	1
Config. 6	21	4800	1200	4800	1200	1	0	0	0
	22	4800	1200	4800	1200	0	1	0	0
	23	4800	1200	4800	1200	0	0	1	0
	24	4800	1200	4800	1200	0	0	0	1
Config. 7	25	3000	3000	3000	3000	1	0	0	0
	26	3000	3000	3000	3000	0	1	0	0
	27	3000	3000	3000	3000	0	0	1	0
	28	3000	3000	3000	3000	0	0	0	1

Figure 1.5 shows the distribution of tracer in the reservoir when 3000 m³/day had been injected into each injector over a period of 300 days (i.e. runs 25-28).

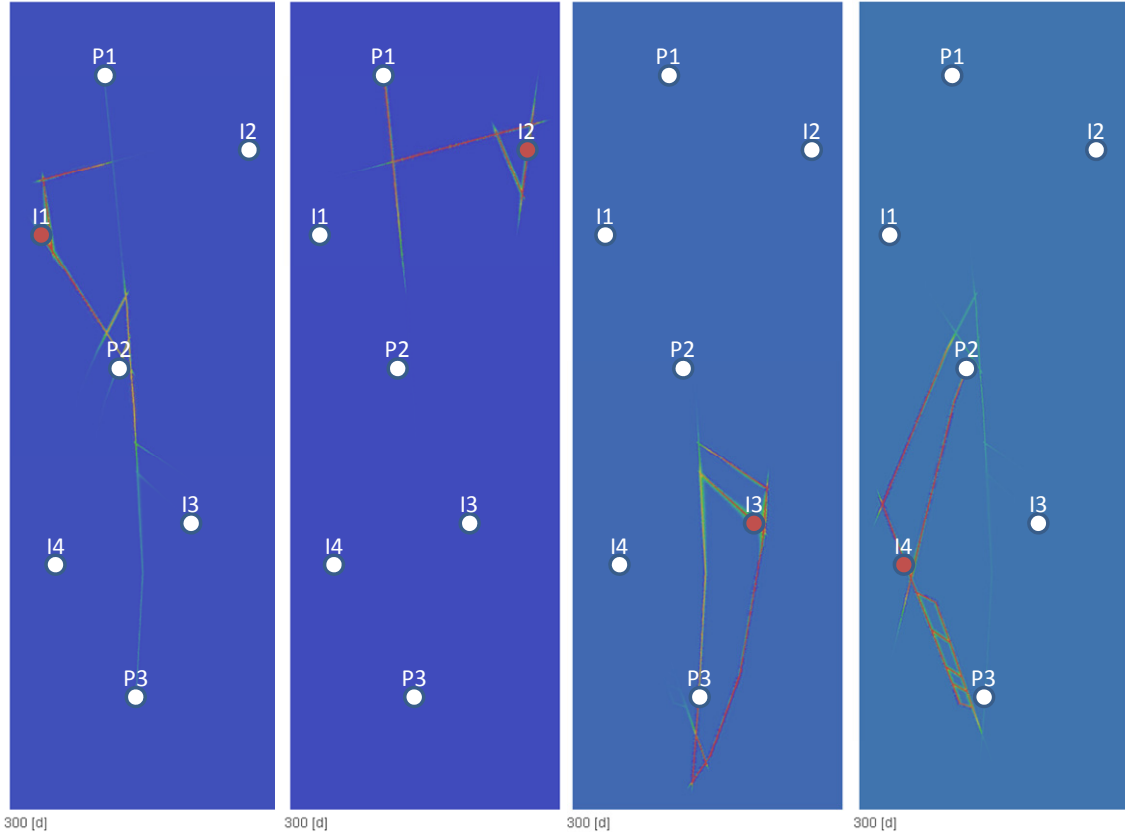


Figure 1.5: The tracer distribution in the reservoir after 300 days of tracer injection, into wells I1 through I4, going from left to right.

The well configuration resulted in 12 possible injector-producer connections. The tracer returns for each connection, at each of the seven flow configurations is shown in Figure 1.6. It is clear from these results that the tracer returns can vary significantly as a function of the injection rate configuration. The variation can occur in terms of the mean arrival time, the tracer dispersion, and the fraction of the initial concentration recovered. To account for the first two, we suggest viewing the responses in terms of the cumulative flow going from each injector to each producer.

To be able to compute the cumulative flow one must have an estimate of the flow rate going from each injector to each producer. One way to estimate this quantity is to compute the relative concentration of injectate eventually arriving at each producer, and equating that to the fraction of injection water arriving at the producer. That is:

$$\frac{C_{IiPj}(t_f)}{C_{Ii}} = w_{ij} = g_{ij} \frac{q_{Ii}}{q_{Pj}} \quad (0.3)$$

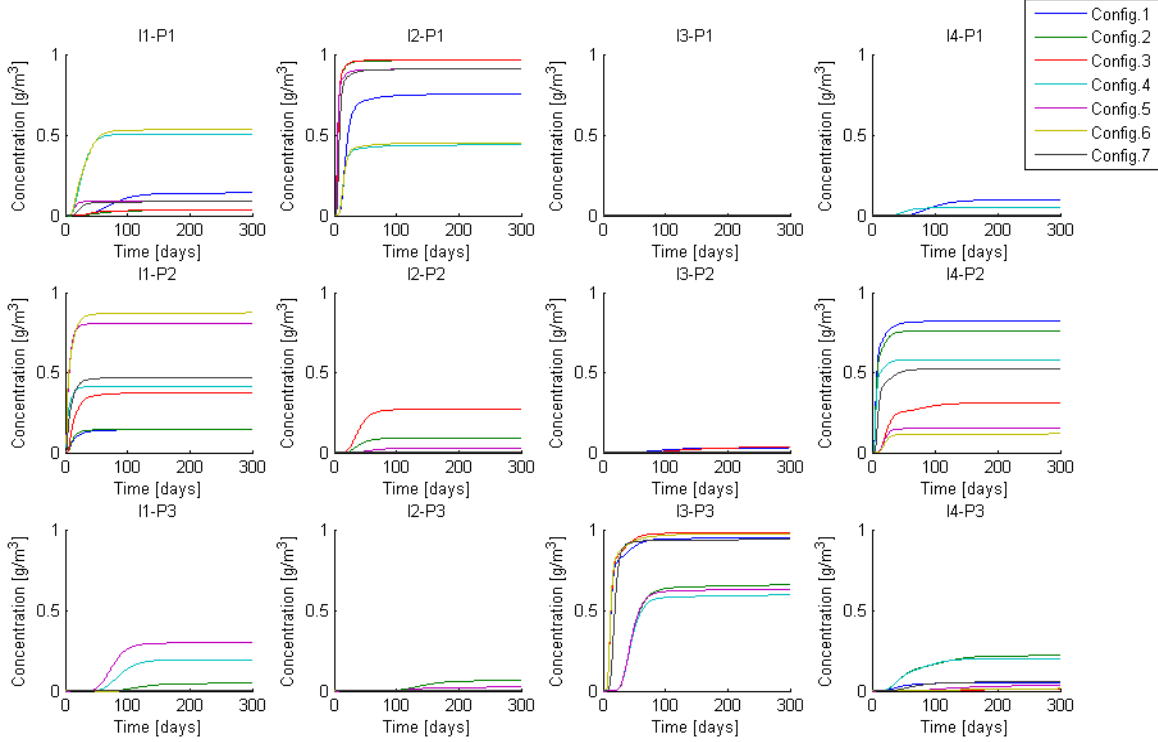


Figure 1.6: An illustration of the tracer returns coming from each injector to each producer under various injection rate configurations.

where C denotes concentration, q denotes injection rate, t_f is the last measurement time, and g is the fraction of injection water arriving at the producer. This fraction will be referred to as the tracer based interwell connectivity. Note that the estimate of g may vary depending on the injection rate configuration. The cumulative flow for each injector producer pair would then be:

$$Q_{ij} = g_{ij} q_{i,t} t \quad (0.4)$$

where t denotes the time from the beginning of tracer injection.

The tracer based interwell connectivity was compared to the flow rate based connectivity. An additional simulation with step wise varying flow rates had to be run to compute the flow rate based connectivity. Further discussion on how to compute the flow rate based connectivity can be found in Lee et al. (2010) and in the quarterly reports of Summer and Fall 2010. The flow rate based and tracer based interwell connectivities are compared in Figure 1.7. From this comparison it is apparent that the tracer based interwell connectivity is generally more extreme than the flow rate based interwell connectivity. We suppose that this is because the flow rates are affected more by the pressure (or diffusion) equation while the tracer travels mostly in an advective manner, i.e. along the main flow paths. A relatively large variability in the tracer based interwell connectivity as a function of the injection rate configuration is also observed in Figure 1.7, although we believe that some

of this variability may be attributable to insufficient simulation time and numerical inaccuracy in the simulations.

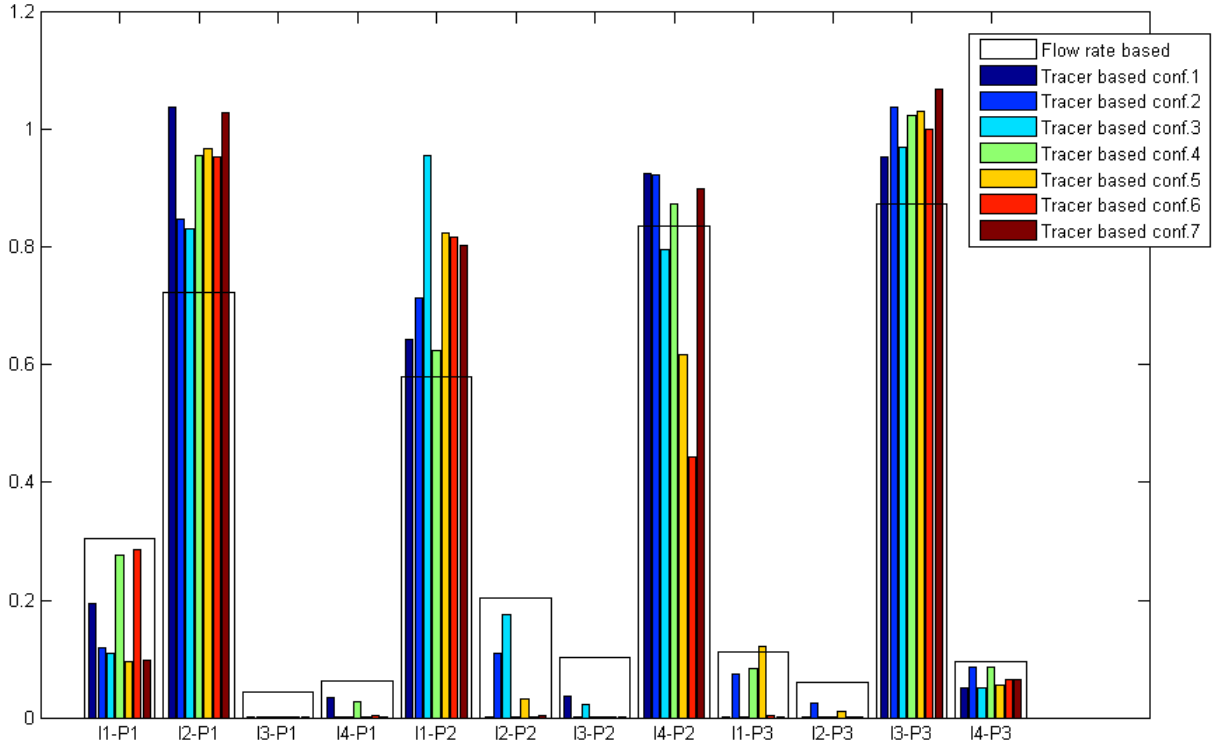


Figure 1.7: A comparison of the flow rate based interwell connectivity and the tracer based interwell connectivity.

The variability in the ultimate concentration of tracer recovered occurs because of dilution by flow streams coming from the other injectors or the reservoir itself. To account for this variability we normalized the concentration by the last measured concentration value, i.e.:

$$C_{iPj}^N(t) = \frac{C_{iPj}(t)}{C_{iPj}(t_f)} \quad (0.5)$$

These normalized concentration values are plotted in Figure 1.8 as a function of the cumulative flow computed from Equation (0.4). It is noticeable that the return curves for the stronger well connections (e.g. I2-P1, I1-P2, I4-P2 and I3-P3) coincide more accurately after this normalization, than do those that have weak connections (e.g. I1-P3 and I2-P3). A plausible explanation is that the interaction between these wells is dominated by one (or possibly two) flow paths, and therefore the one-dimensional advection-dispersion provides a relatively good approximation of the tracer returns (see further discussion in the quarterly report of Fall 2010). This information is important because it indicates that by performing a tracer test at one set of injection rates, one might expect to be able to predict what the tracer returns would be at another set of injection rates. This is especially true for the

strongest well-to-well connections, which are usually the most important ones when it comes to utilizing this information.

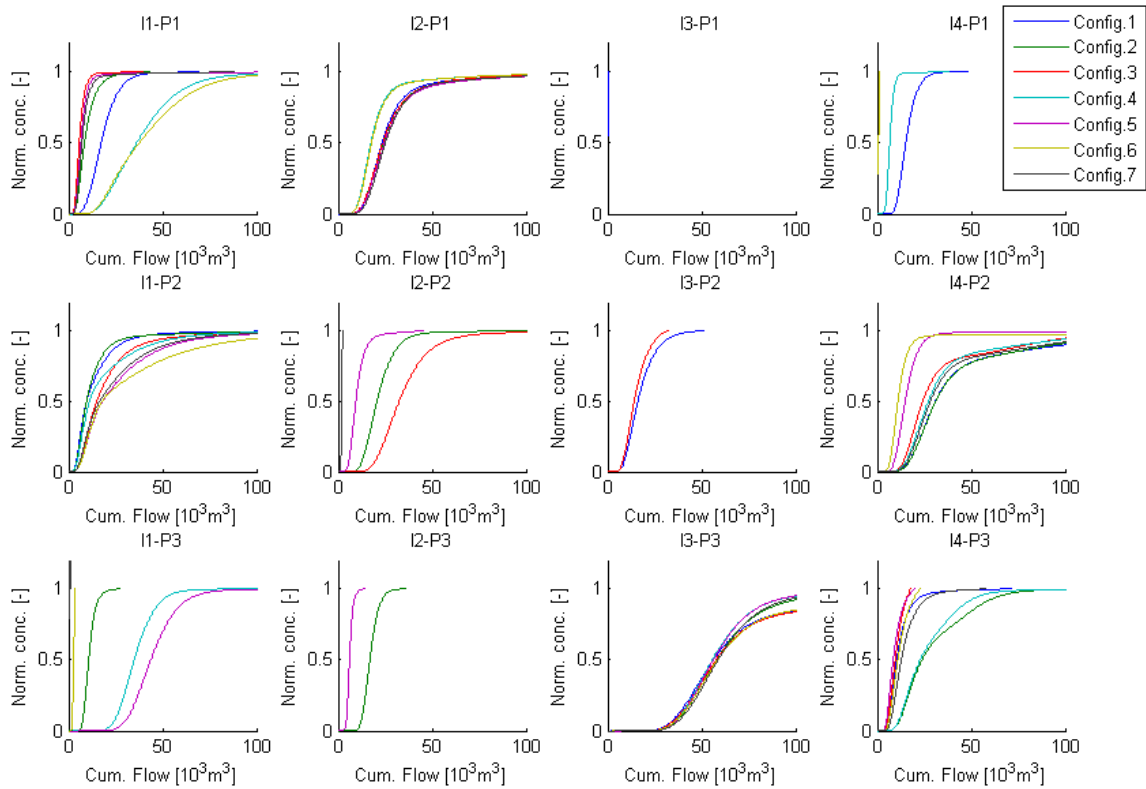


Figure 1.8: Normalized tracer returns as a function of an estimate of the cumulative flow passed between an injector-producer pair. The cumulative flow is based on an interwell connectivity estimate computed from each tracer return.

The cumulative flow based tracer kernels that were discussed in the quarterly report of Fall 2010 were computed from the normalized step responses as

$$\kappa_{ij}(Q_{ij}) = \frac{\partial C_{iPj}^N}{\partial Q_{ij}} \quad (0.6)$$

The tracer kernels are shown in Figure 1.9. An average of the tracer kernels is shown by a blue dashed line. This can be compared to the response with all injection rates equal, shown by a black dashed line. Each one of these average responses was used to estimate the average pore volume for each connection. The volume was computed from the moment equation.

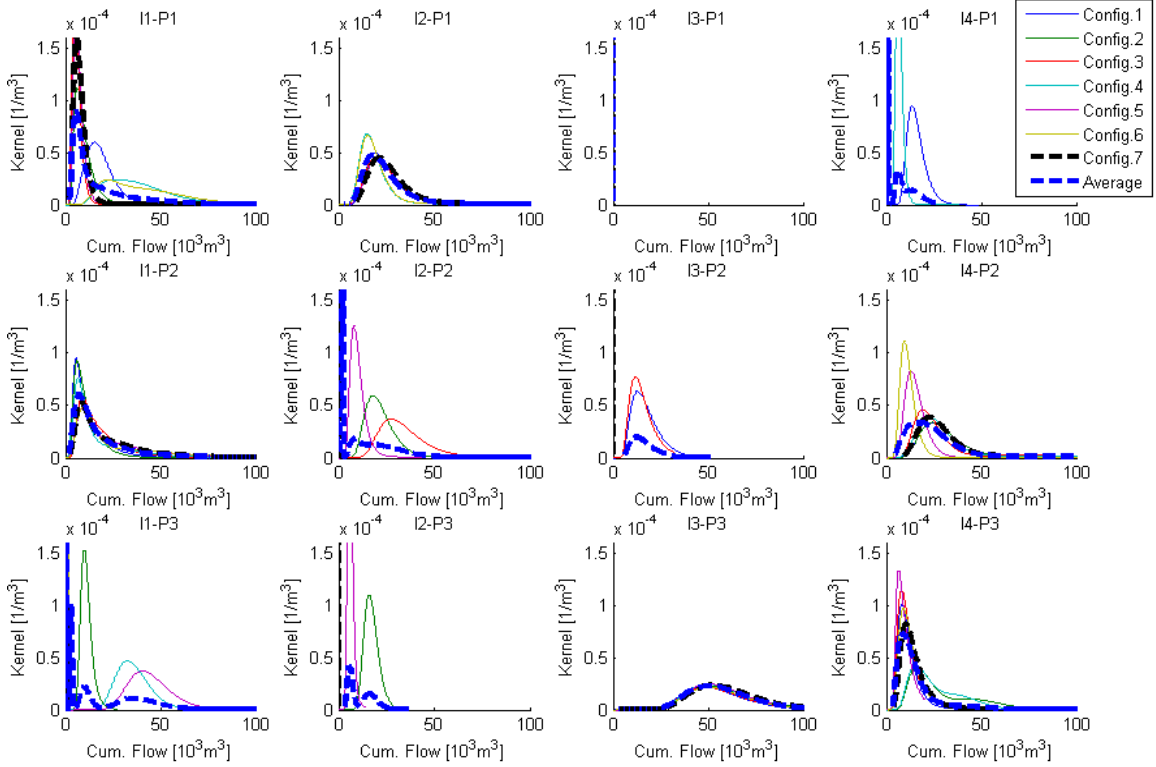


Figure 1.9: Tracer kernels computed for each of the injector-producer connections based on continuous injection tracer test at various injection rate configurations.

$$V_{x,ij} = \frac{\int_0^{Q_{ij}(t_f)} \tilde{Q}_{ij} \kappa_{ij}(\tilde{Q}_{ij}) d\tilde{Q}_{ij}}{\int_0^{Q_{ij}(t_f)} \kappa_{ij}(\tilde{Q}_{ij}) d\tilde{Q}_{ij}} \quad (0.7)$$

The resulting volume estimates are shown in Table 1.2 and Table 1.3. Note that when there is poor connectivity between the wells, this method tends to underestimate the volume between the wells. This is because in some cases no (or very little) tracer had been delivered along the connection over the 300 day testing period used in the simulation study. This problem is partially accounted for by averaging the responses which is why more reasonable estimates are found using that method than just the tracer returns from configuration 7. Nevertheless, it is obvious, e.g. by observing Figure 1.4, that there is a fracture connection of large volume between I3 and P1. As very little tracer was passed along that connection at the injection rate configurations considered here, this led to the obvious underestimates shown in Table 1.2 and Table 1.3. Thus the volume estimates are dependent on what the specific flow configuration is, since flow can travel along different flow paths at different configurations. Erroneous estimates of this kind need to be corrected by insight, i.e. knowing that if a very small fraction of tracer was returned, that probably means that there was a very large pore volume separating the two wells or that the interwell connectivity was very low.

Table 1.2: Estimated pore volume of each injector-producer connection, as computed from the average response of all simulated injection rate configurations. The color coding refers to the presumed quality of the estimates; red is poor, yellow is medium and green is good. Volume estimates are in m^3 .

Vx	I1	I2	I3	I4
P1	19,052	28,920	405	7,972
P2	22,018	17,719	16,413	34,272
P3	18,864	11,796	71,227	16,432

Table 1.3: Estimated pore volume of each injector-producer connection, as computed from the response with all injection rates equal (Config. 7). The color coding refers to the presumed quality of the estimates; red is poor, yellow is medium and green is good. Volume estimates are in m^3 .

Vx	I1	I2	I3	I4
P1	8,367	32,691	0	1
P2	24,903	1,848	17	41,235
P3	241	1	65,371	14,676

1.5 OPTIMIZATION OF INJECTION SCHEDULING

Utilizing tracer data to optimize injection strategies in geothermal reservoirs was discussed by Lovekin and Horne (1989). Several publications by Shook (2001; 2003; 2004) also discuss the potential application of tracer data to infer reservoir properties that could be used to optimize injection schedules. Methods for predicting thermal breakthrough in fractured reservoirs based on information interpretable from tracer tests have also been discussed by Lauwerier (1955), Gringarten and Witherspoon (1975), Bodvarsson and Pruess (1984), Kocabas (2005), and Wu et al. (2008). In this section we build on the work of these authors to develop a method for optimizing reinjection schedules.

In developing the optimization problem we considered three possible objective functions. The formulations involved are covered briefly, and followed by short examples of their application.

1.5.1 Minimizing mass production

For the first method we considered relying solely on the tracer returns with the aim of finding the injection schedule that minimizes the total mass produced over a given time period. The objective function in this case was:

$$O(\bar{q}_I) = \sum_{j=1}^{N_p} \int_0^{t_f} C_{P_j}(t, \bar{q}_I) q_{P_j}(t, \bar{q}_I) dt \quad (0.8)$$

where C_{P_j} represents the produced concentration in well j from a continuous tracer injection into all injection wells. A challenge with this model was to determine an

appropriate end time t_f , since the tracers would arrive at far earlier times than would the corresponding thermal front. Letting t_f extend over periods much longer than the tracer arrival time (e.g. a project life of 30 years) gave results that were prone to error, because the tracer transient would only cover a small part of the overall production period.

An example with two injection wells and two production wells was used to test the application of the method. A reservoir model, with x and y dimensions of 1000 m and a height (in the z dimension) of 500 m, was created. Three vertical fractures were placed in the model, connecting the wells as shown in Figure 1.10. Each fracture was given an aperture of 1 m, height 500 m and porosity 5%. The distance between wells I1 and P1 (or I2 and P2) was 600 m and between I1 and P2 was 750 m.

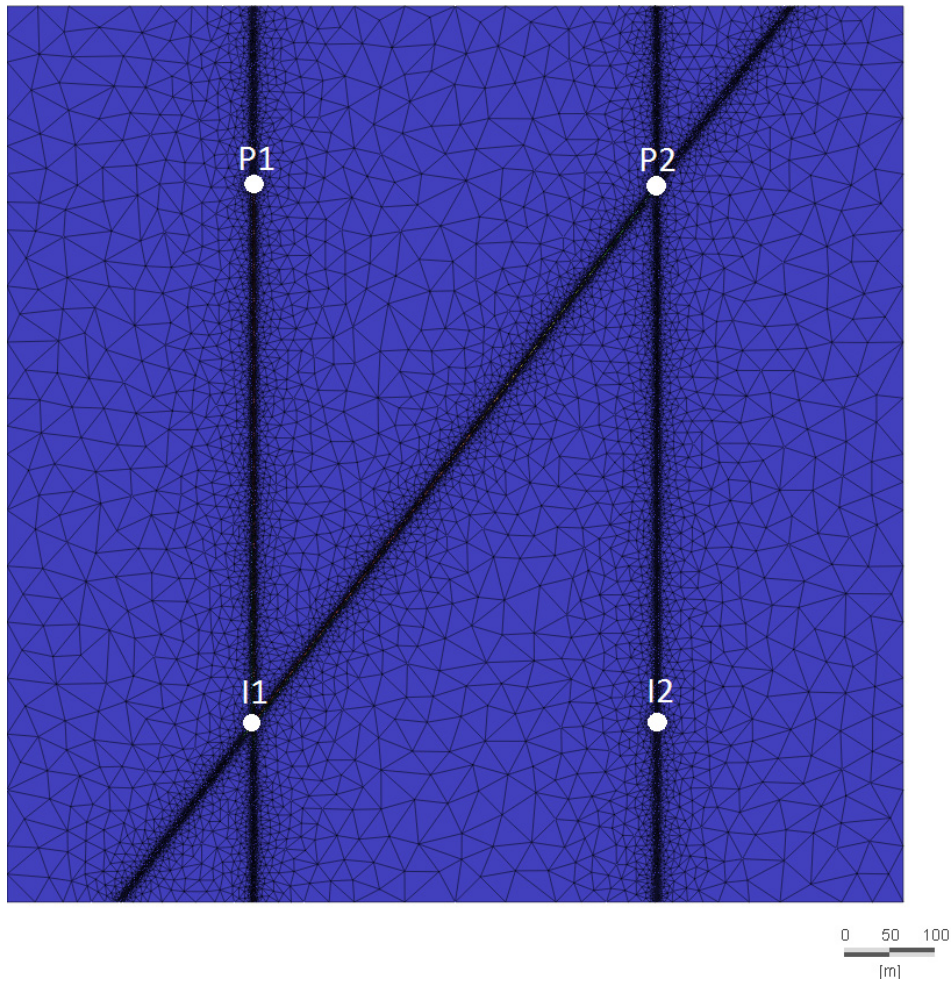


Figure 1.10: The configuration of wells and fractures in a test case used to investigate the possibility of optimizing reinjection scheduling based on tracer returns.

Simulations of continuous tracer injection were performed, with an injection rate of 2500 m^3/day into each well. The smallest grid blocks were around 2 m in the direction of flow, and the largest flow velocity was around 100 m/day. To limit numerical dispersion we limited the time step to 0.02 days and used the shock capturing flow transport option in

FEFLOW. We also used a dispersion coefficient of 50 m in the longitudinal direction and 5 m in the transverse direction. The resulting tracer returns were used to compute the tracer kernels shown in Figure 1.11. These tracer kernels could then be used to compute C_{Pj} in Equation (0.8) as a function of the injection rates.

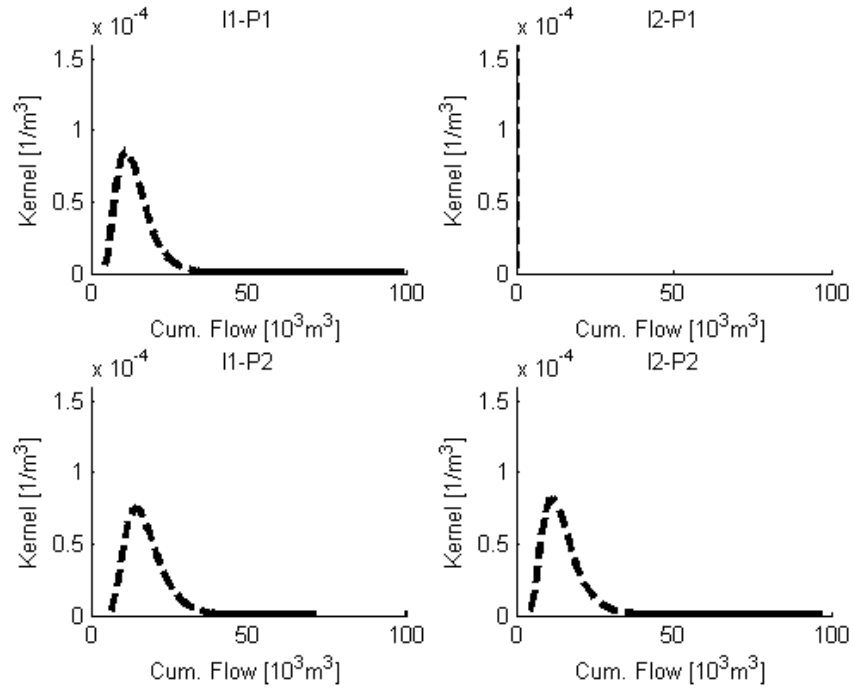


Figure 1.11: Tracer kernels derived from the flow model presented in Figure 1.10. Note that the kernel representing the connection between I2 and P1 is virtually zero because no tracer was delivered along that path. A kernel derived from an analytical equation with a very large volume was used to account for this anomaly when running the optimization algorithm.

The optimum injection schedule determined from this method was to assign 64% of the injected fluid to well I1 and 36% to well I2. Figure 1.12 shows the objective function along with the chosen constraints on the total injection rate and the maximum injection rate assigned for each well. The final time, t_f , used in this case was 20 days. Note that for larger flow rates (or a larger final time) the objective function gets less sensitive to the injection rate. This is because the production concentration will be essentially the same as the injected concentration for most of the time period under consideration.

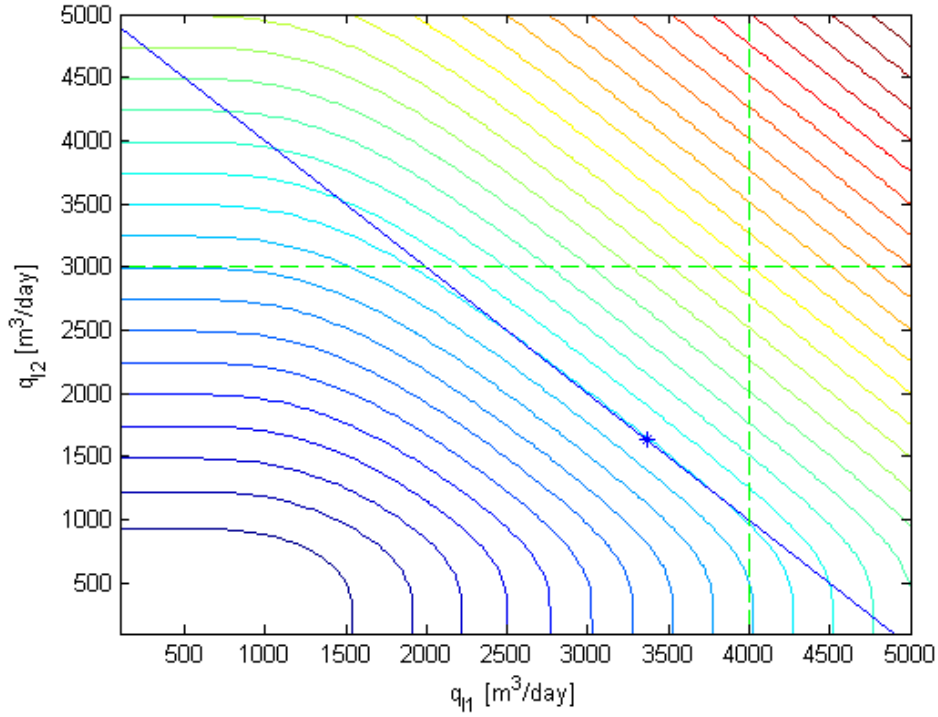


Figure 1.12: A contour plot of the objective function based on mass production. A constant total injection constraint of 5000 m³/day is illustrated by the blue diagonal line. Maximum injection constraints of 4000 and 3000 m³/day for injectors I1 and I2, respectively, are shown by the green dashed lines. The optimum feasible point is shown by the blue star.

1.5.2 Maximizing energy extracted

The second method considered was to attempt to maximize the energy extracted from the reservoir. The objective function in this case was defined as:

$$O(\bar{q}_I) = \sum_{j=1}^{N_p} \int_0^{t_f} \rho \Delta h_{p_j}(t, \bar{q}_I) q_{p_j}(t, \bar{q}_I) dt \quad (0.9)$$

where ρ represents the density of the produced fluid (assumed to be constant). The change in enthalpy was modeled as:

$$\Delta h_{p_j}(t, \bar{q}_I) = \rho c_w (T_{p_j}(t, \bar{q}_I) - T_I) \quad (0.10)$$

where c_w represents the specific heat capacity of water (assumed constant) and T_I is a constant injection temperature. The production temperature at producer j would be:

$$T_{p_j}(t, \bar{q}_I) = \sum_{i=1}^{N_I} w_{ij} T_{ij}(t, \bar{q}_I) = \sum_{i=1}^{N_I} w_{ij} (T_0 - (T_0 - T_I) T_{D,ij}(t, q_{I_i})) \quad (0.11)$$

where T_0 is the initial temperature in the reservoir and $T_{D,ij}$ represents the a function of dimensionless temperature change as reported by most of the previously mentioned authors that have discussed thermal breakthrough in fractured reserovirs. For example, using Lauwerier's (1955) formulation

$$T_{D,ij}(t, q_{I_i}) = \operatorname{erfc} \left\{ \left(\frac{(\rho_a c_a)^2}{K_r \rho_r c_r} \left(\frac{\phi b q_{ij}}{V_{x,ij}} \right)^2 \left(t - \frac{\rho_a c_a V_{x,ij}}{\rho_w c_w \phi q_{ij}} \right) \right)^{-0.5} \right\} \quad (0.12)$$

where b denotes the fracture aperture, ϕ is the fracture porosity, K_r is the thermal conductivity of the rock and the group

$$\rho_a c_a = \phi \rho_w c_w + (1 - \phi) \rho_r c_r \quad (0.13)$$

where the subscript r refers to the rock properties. The parameter w_{ij} in Equation (0.11) denotes the mixing weight given by Equation (0.3).

Most of the thermodynamic parameters Equation (0.12) can be estimated fairly accurately based on existing knowledge of the geology and reservoir fluid. The largest uncertainties are related to the geometry of the flow paths. The pore volume $V_{x,ij}$ and flow rate q_{ij} can be estimated from the tracer methods discussed in section 1.4, but methods to determine the group ϕb have not been well established. Moreover, the Lauwerier solution assumes flow through a single fracture surrounded by a matrix of infinite size.

The same example as described in Section 1.5.1 was used to test this method. The pore volumes estimated from the tracer kernels are shown in Table 1.4. A zero volume estimate was found for the I2-P1 connection because no tracer was transported from injector 2 to producer 1. This was accounted for in the optimization by assuming there was a very large volume separates the two wells, thereby leaving the optimization problem indifferent to this connection.

Table 1.4: Estimated pore volume of flow paths connecting wells in the model shown in Figure 1.10. The estimates are based on tracer tests. The estimate for the I2-P1 connection is poor because no tracer was transported along that connection.

Vx	I1	I2
P1	14,122	0
P2	17,522	14,881

The optimal injection schedule determined using this method was similar to what was seen in the previous case. Approximately 67% of the fluid was assigned to injector I1 and 33% to I2. The objective function along with the constraints and optimal point are shown in Figure 1.13.

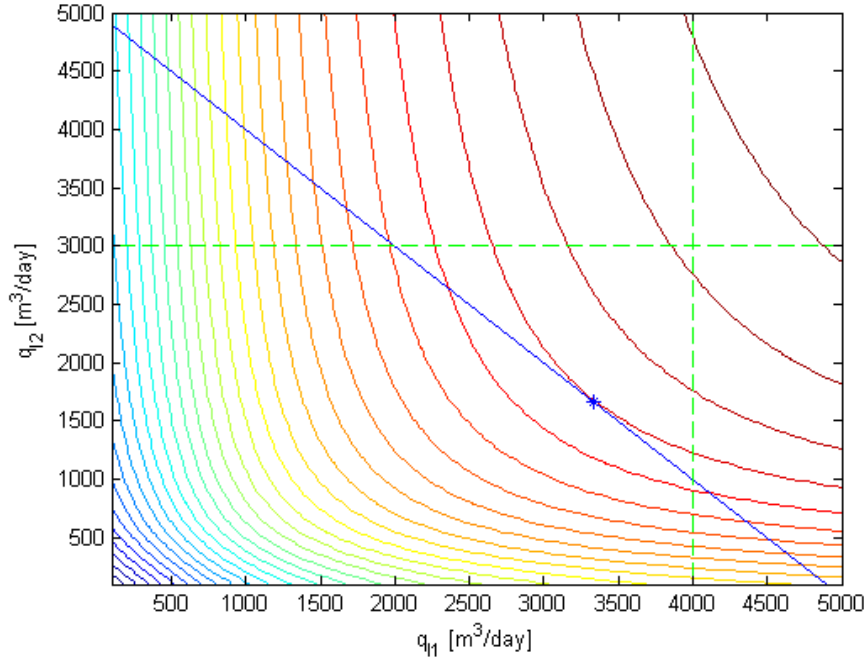


Figure 1.13: A contour plot of the objective function based on energy extraction. A constant total injection constraint of $5000 \text{ m}^3/\text{day}$ is illustrated by the blue diagonal line. Maximum injection constraints of 4000 and $3000 \text{ m}^3/\text{day}$ for injectors I1 and I2, respectively, are shown by the green dashed lines. The optimum feasible point is shown by the blue star.

The success of this optimization method depended on how well the thermal breakthrough could be predicted by the analytical heat transfer equations. To investigate this we compared $T_P(t)$ as predicted by Equation (0.11) to simulated values. Comparisons were made with equal injection into each injector (Figure 1.14) and at the optimal injection configuration (Figure 1.15). In this simple case the Lauwerier solution provides a relatively accurate estimate of when the thermal front will arrive. Note, however, that the parameter group ϕb was assumed to be known here. This usually is not the case. An even better match could probably be obtained using more complex models, such as those derived by Gringarten and Witherspoon (1975) or (Wu et al., 2008). For most practical cases, this would likely involve having to tune some of the unknown parameters of those models to fit the temperature data as it becomes available. Better estimates for these unknown parameters could also be obtained by other means such as seismic surveying, wellbore imaging or tracer tests with reactive tracers.

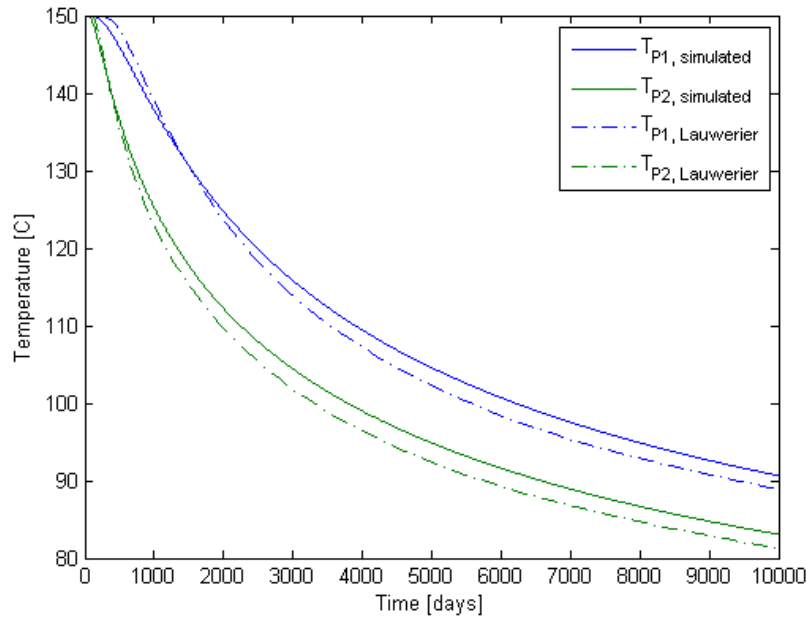


Figure 1.14: Comparison of simulated thermal breakthrough and thermal breakthrough as predicted by the Lauwerier (1955) analytical model. For this case water at 50 C is injected at 2500 m³/day into each of the two injectors.

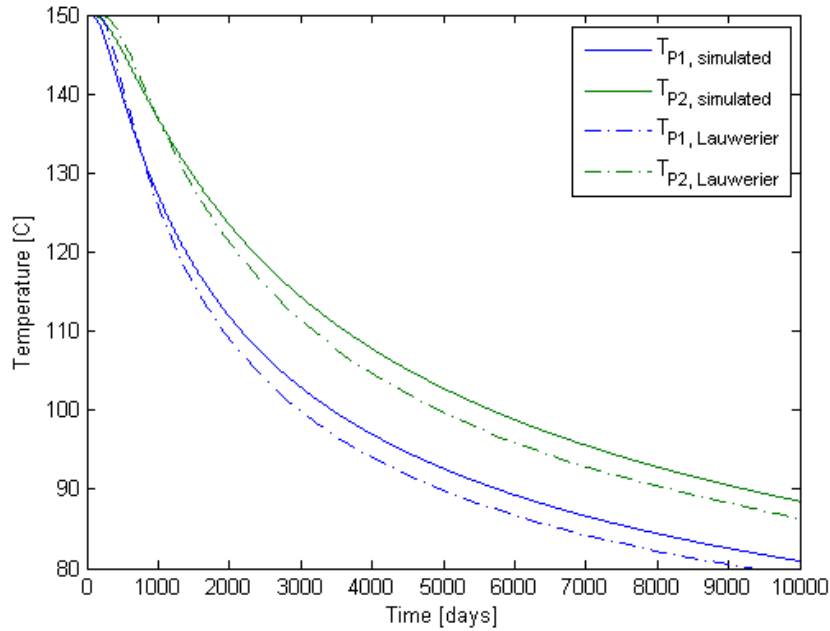


Figure 1.15: Comparison of simulated thermal breakthrough and thermal breakthrough as predicted by the Lauwerier (1955) analytical model. For this case water at 50 C is injected at the optimal allocation of 3366 m³/day into injector I1 and 1634 m³/day into I2.

It is interesting to note that the thermal fronts do not arrive at the same time at the optimal configuration as one might have suspected at first glance. Instead the flow rates are tuned such that the well with the higher flow rate (P2) stays hot over a longer time period.

1.5.3 Maximizing net present value of production

The final model we considered was to maximize the net present value of production from the reservoir. To do this we used an empirical correlation between injection and production temperature and power output. The correlation, found by Bennett and Horne (2011) based on results presented in the MIT report (Tester et al., 2006, Figure 7.3), follows.

$$z_j(T_{P_j}, T_I) = 3.854 \times 10^{-5} (T_{P_j} - \zeta)^2 - 1.268 \times 10^{-3} (T_{P_j} - \zeta) - 2.123 \times 10^{-2} \quad (0.14)$$

Here z_j is the specific power output of producer j [kW/(m³/day)], and

$$\zeta = 0.563T_I - 14.51 \quad (0.15)$$

The temperatures are in degrees Celcius. Water density was assumed to be 900 kg/m³.

The net present value of producing from the reservoir was then computed as

$$O(\bar{q}_I) = \sum_{j=1}^{N_P} \int_0^{t_f} P(t) z_j(T_{P_j}(t, \bar{q}_I), T_I) q_{P_j}(t, \bar{q}_I) e^{-rt} dt \quad (0.16)$$

where $P(t)$ denotes the unit price of energy and r denotes the chosen discount rate for the investment. T_{P_j} was computed using Equation (0.11).

Using this method to find the optimal injection rate allocation yielded a 70% injection into well I1 and 30% in I2. The objective function and constraints are shown in Figure 1.16. The increase in the objective function from the initial guess (where all injection rates were equal) was approximately 6%. This result was obtained assuming an interest rate $r=8\%$ and an energy price, increasing over a 30 year period in real terms, from 60 to 120 \$/kWh with an added 2% inflation. Running the optimization with alternative assumptions about the price and interest rate showed that the optimal allocation does not depend much on these figures.

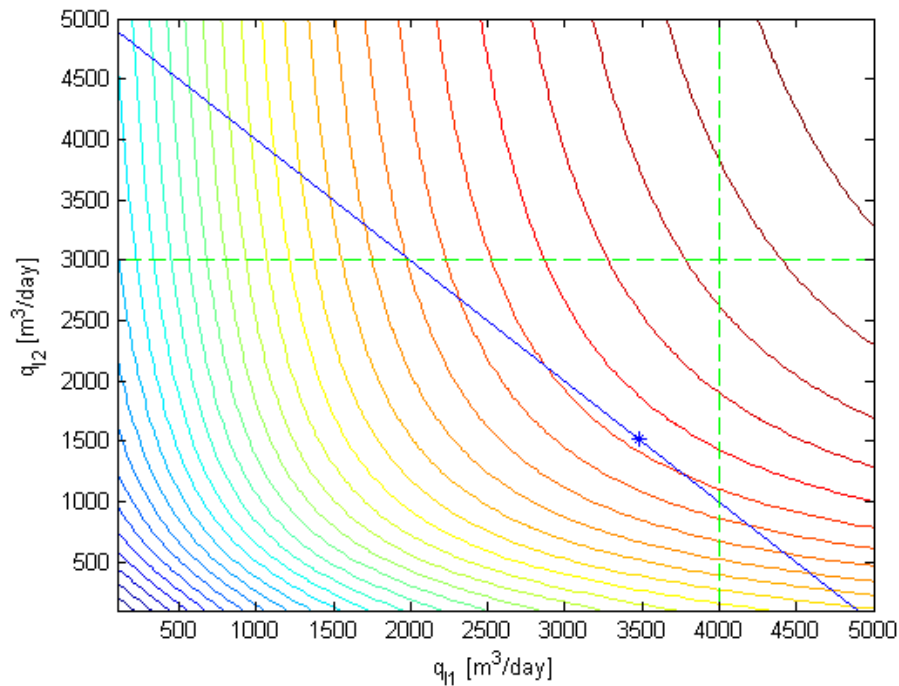


Figure 1.16: A contour plot of the objective function based on net present value of production. A constant total injection constraint of $5000 \text{ m}^3/\text{day}$ is illustrated by the blue diagonal line. Maximum injection constraints of 4000 and $3000 \text{ m}^3/\text{day}$ for injectors I1 and I2, respectively, are shown by the green dashed lines. The optimum feasible point is shown by the blue star.

1.6 FUTURE WORK

In this report we have discussed the development of a two-dimensional discrete fracture flow model, based on data from the Soultz enhanced geothermal system. A number of tracer transport simulations were performed using this model with a number of additional injection and production wells. These data will be used to obtain estimates of the optimal reinjection schedule for that reservoir model, using the objective functions described in Section 1.5. Moreover, we will investigate the possibility of running the same example with a fully three-dimensional discrete fracture model.

The optimization procedures described in this report rely on a mapping of values obtained from tracer tests to estimate the thermal breakthrough in the production well. In most cases the tracer tests do not fully suffice to estimate the thermal breakthrough because important information e.g. about the fracture spacing and the area available for heat transfer cannot be obtained from the tracer tests. Thus other data sources should be considered to constrain these parameters further. Pressure and flow rate data might be useful. Our analysis has also revealed that the optimization is most sensitive to the largest fracture connections, which means that the important fractures might be viewable in seismic surveys or with wellbore imaging tools.

A slightly different approach would be to tune the unknown parameters of the thermal breakthrough model being considered (using a nonlinear parameter estimation routine) as the thermal breakthrough data becomes available. This describes a dynamic optimization problem (although the dynamics are very slow) and would require an estimate of the state of each injector-producer connection as a function of time and space.

2. FRACTURE CHARACTERIZATION OF ENHANCED GEOTHERMAL SYSTEMS USING NANOPARTICLES

This research project is being conducted by Research Associates Mohammed Alaskar and Morgan Ames, Senior Research Engineer Kewen Li and Professor Roland Horne. The objective of this study is to develop in-situ multifunction nanosensors for the characterization of Enhanced Geothermal Systems (EGS).

2.1 SUMMARY

During this quarter we began investigation of nanoparticle flow in fractures. The injection of silicon dioxide (SiO_2) nanoparticles was conducted to explore the nanoparticle mobility through the fractured greywacke core from The Geysers. The silicon dioxide nanoparticle size was 350 nm with negative 73 mV surface charge. The nanoparticles were identified in the effluent using scanning electron microscopy (SEM) imaging and dynamic light scattering (DLS). The return curve of the nanoparticles was not determined because the concentration of injected nanofluid or effluents were not known. The permeability of the core sample dropped significantly following the injection of the nanoparticles.

Three fluorescent silica microsphere samples of different sizes and colors were purchased from CorpuScular Inc., New York, USA. These were 1 μm blue fluorescent, 4 μm green fluorescent and 10 μm red fluorescent silica microspheres. The microsphere samples were characterized in terms of size, shape, zeta potential and fluorescence emission spectra. It was found that the size of the blue microspheres was 2 μm with an average surface charge of positive 15.4 mV. The green microspheres sample was monodisperse with an average size of 5 μm . There was a considerable difference (from -80.2 to +35.3 mV) in zeta potential measurements among diluted samples of the green microspheres, which might be attributed to the settlement of the microspheres during the zeta potential measurement. The red microsphere sample was polydisperse with wide particle size range between 5 and 26 μm .

A second investigation this quarter continued the consideration of temperature-sensitive tin-bismuth nanoparticles. Experiments last quarter had shown some difficulty in transporting these nanoparticles through a Berea sandstone core, although they passed successfully through a glass-bead pack. The tin-bismuth sample that was synthesized in the previous quarter was characterized using DLS, and was found to have a wide particle size distribution. In an attempt to obtain a sample with a narrower size distribution and particles smaller than 200 nm, centrifugations of this sample were performed at several centrifugation speeds. DLS measurements were performed on the resulting samples, and it was found that while narrower size distributions were achieved, particles larger than 200 nm were still present. Also, the resulting sample was very dilute. For these reasons, the sonochemical synthesis of tin-bismuth nanoparticles was repeated at the highest possible sonication power with the expectation of obtaining a sample with a greater number of small (<200 nm) nanoparticles. This sample was also centrifuged to separate large particles. The original and centrifuged samples were characterized using DLS.

2.2 INTRODUCTION

Last quarter (Oct. – Dec., 2010), the injection of iron oxide (Fe_2O_3) nanoparticles coated with the surfactant polyvinylpyrrolidone (PVP) was conducted to explore the nanoparticles mobility through slim tube packed with glass beads. Surfactant coating of iron oxide nanoparticles modified their surface charge. Both the nanoparticles and flow medium have negative charge. Coated iron oxide nanoparticles were identified in the effluent using scanning electron microscopy (SEM) imaging. The concentrations were determined by measuring their absorption using UV-vis spectrophotometry. The return curve showed that about 23% of injected nanoparticles were recovered. Spherical silver nanoparticles were injected into Berea sandstone. The silver nanoparticles were identified in the effluent samples and only 25% of injected nanoparticles were recovered. Post-injection of pure water at higher injection rates and backflushing of the core sample did not result in additional recovery of the silver nanoparticles and all effluents were free of nanoparticles.

Tin-bismuth nanoparticles were injected into Berea sandstone and into a tube packed with glass beads. It was found that tin-bismuth nanoparticles can be recovered following their injection into the tube packed with glass beads without being trapped within the flow conduits, but not through the pore network of the Berea sandstone. During the core injection, the tin-bismuth nanoparticles were identified in a few effluent samples at low concentrations. It was observed that smaller nanoparticles (200 nm and smaller) were transported through the pore spaces of the rock. Backflushing showed that there was entrapment of nanoparticles, including sizes greater than 200 nm. This might be attributed to an affinity of these nanoparticles to the sandstone rock matrix or high nanoparticle concentration imposing constraints to their flow. Mobility of the tin-bismuth nanoparticles in the absence of rock material was tested by their injection into the tube packed with glass beads. It was found that the tin-bismuth nanoparticles of all sizes flowed through the slim tube.

The sonochemical synthesis of tin-bismuth nanoparticles was repeated in less viscous oil in an attempt to achieve a more uniform particle size distribution, and the sample was characterized using SEM. A monodisperse sample should allow more conclusive demonstration of the size change sensing mechanism and may even aid their transport through rock. However, the size distribution of this sample was still wider than desired.

During this quarter, a naturally fractured greywacke core from The Geysers was prepared for the injection of fluorescent silica microspheres. The preparation of the fractured core included the estimation of the hydraulic aperture and permeability of the fracture. The fluorescent silica microsphere samples were characterized in terms of size, shape, zeta potential and light emission using optical and scanning electron microscopy, zetasizer and fluorescence spectrometer, respectively. Prior to the injection of the silica microsphere, silicon dioxide nanoparticles were characterized and injected into the fractured core as a base-line measurement. The effluents were analyzed using DLS and SEM.

Also this quarter, the tin-bismuth sample that was synthesized in the previous quarter was characterized using DLS. Centrifugations of this sample were performed at several

centrifugation speeds, and the resulting samples were characterized using DLS. The sonochemical synthesis of tin-bismuth nanoparticles was repeated at the highest possible sonication power for the mineral oil used, with the expectation of obtaining a more ideal sample. This sample was also centrifuged to separate large particles from the sample. The original and centrifuged samples were characterized using DLS.

2.3 EXPERIMENTAL SETUP AND CHARACTERIZATION OF FRACTURED GREYWACKE

This section describes the experiments and the standard measurement of porosity, permeability, pore volume and fracture hydraulic aperture of the fractured greywacke.

The core sample tested was a fractured greywacke from The Geysers geothermal field, with 5.08 cm diameter and 3.01 cm length (Figure 2.1). The core sample was fitted between the two end-pieces and wrapped with Teflon shrink tube. An electric heating gun was used to bond the assembly together. To achieve proper sealing, the heat was applied evenly starting bottom up in round motion. The assembly was positioned horizontally and polyethylene tubes (0.3175 cm in diameter) and fittings were used to connect the water pump and pressure manometer to the core assembly (Figure 2.2). Since only a very low differential pressure was required to flow fluid through the fractured core, the inlet pressure was measured using a manometer tube rather than a transducer. The flow rate was measured using a balance and stop watch.

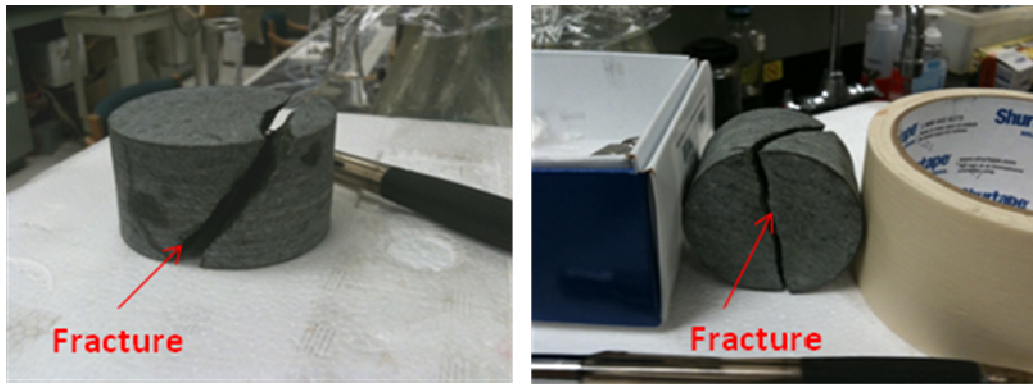


Figure 2.1: Fractured greywacke core sample.

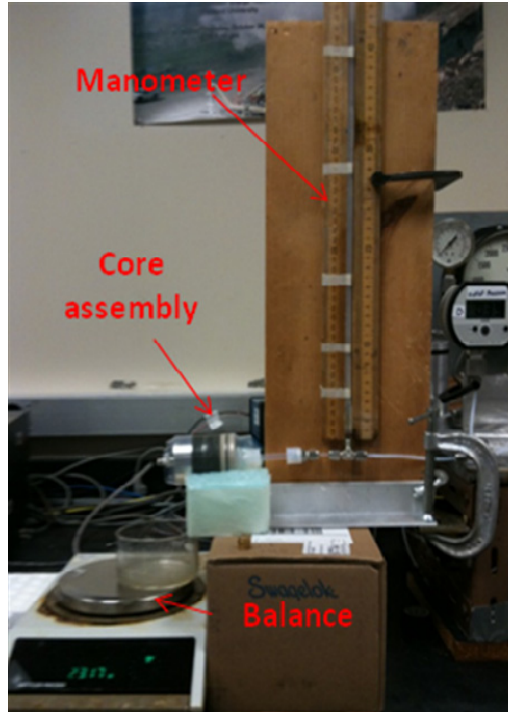


Figure 2.2: Experimental setup for hydraulic aperture and permeability measurements of fractured greywacke rock sample.

Prior to saturation, the core was dried at 75°C under vacuum pressure of 0.09 MPa for about 3 days, using a vacuum oven. Then, the core and related system were saturated with dionized water. Initially, the system was evacuated using a vacuum pump under vacuum pressure of about 13 millitorr for about 4 hours. The vacuum pump was connected to the system from the inlet side of the core. A water column used to saturate the system was attached at the outlet side of the core assembly. The water column was positioned on a scale to observe the weight change and hence the water volume entered the system (Figure 2.3).

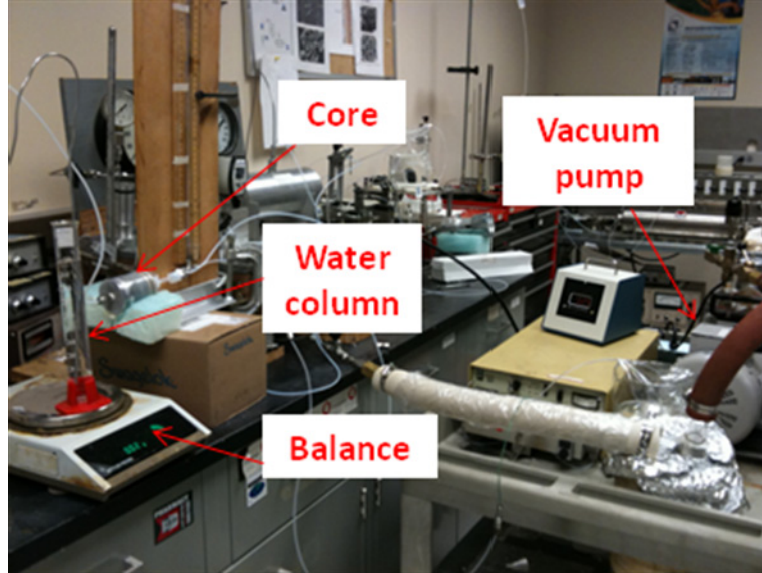


Figure 2.3: Experimental setup during saturation of the fractured greywacke core sample.

The pore volume of the fractured core sample was determined by subtracting the dead volume of connecting tubes, fittings and end pieces from the total volume displaced from the saturation water column. The dead volume of tubes and pore volume were calculated as follows:

$$V_p = V_{total} - V_d \quad (2.1)$$

$$V_{total} = \frac{W_{total}}{\rho_w} \quad (2.2)$$

$$V_d = \pi r^2 l \quad (2.3)$$

Where V_p and V_d are the pore and dead volumes in cubic centimeters, respectively. V_{total} is the total volume of water entering the system in cubic centimeters, W_{total} is the total weight of water entering the system in grams, ρ_w is the density of water in grams per cubic centimeters, l and r are the length and inner radius of tubes, respectively, in centimeters.

Based on the pore volume estimation, the porosity of the core sample was calculated as the ratio of the pore volume to the core bulk volume.

$$\phi = \frac{V_p}{V_B} * 100 \quad (2.4)$$

$$V_B = \pi r^2 l \quad (2.5)$$

where ϕ is the porosity in percentage, V_B is the bulk volume in cubic centimeter, r and l are the radius and length of the core in centimeter, respectively. The core sample was

found to have a pore volume of 1.8 cm³ and porosity of 2.9%. The total volume of water entering the system, dead volume of tubes, dead volume of end pieces, pore volume and porosity are summarized in Table 2.1.

Table 2.1: Summary of bulk, pore, dead volumes and porosity of fractured greywacke core

<i>Measurement</i>	<i>Value (cm³)</i>
Dead volume of tubes	4.2
Dead volume of end pieces	1.75
Total water volume displaced	7.76
Pore volume	1.8
Bulk volume	61.1
Porosity	2.9%

The hydraulic aperture of the fracture was determined using the cubic law. The cubic law is given as:

$$Q = \frac{b^2}{12} \frac{bD\Delta p}{\mu L} \quad (2.6)$$

$$k = \frac{b^2}{12} \quad (2.7)$$

Where Q is the flow rate in cubic meters per second, b is the fracture aperture in meter, D is the fracture width in meter, Δp is the pressure drop across the core sample in Pascal, L is the length of the fracture in meter, μ is the test fluid viscosity in Pascal second and k is the permeability in square meters. The permeability can be expressed in Darcy units using the following conversion

$$1 \text{ darcy} = 9.869 \times 10^{-13} \text{ m}^2 \quad (2.8)$$

The average of the hydraulic aperture of the fracture was found to be approximately 27 μm . The average permeability of the rock was found to be 60 darcy.

2.4 FLUORESCENT SILICA MICROSPHERES: CHARACTERIZATION AND INJECTION EXPERIMENT

The objectives of this experiment were to investigate the transport and recovery of fluorescent silica microspheres through the fracture of the greywacke core sample and study the relationship between the size of recovered microparticles and fracture aperture. As a base-line experiment, initial testing was conducted with injection of silicon dioxide (SiO₂) nanoparticles which we had earlier shown to be transported successfully through Berea sandstone. Silicon dioxide nanoparticles flowed through Berea sandstone core and were not trapped in the pore spaces by hydraulic, chemical or electrostatic effects. Given that the silicon dioxide nanoparticles had been transported successfully through Berea sandstone, our first step in the fracture experiments was to test their delivery through the fractured greywacke core sample. The purpose was to verify if greywacke core material

would impose any constraint on the recovery of silica based nanoparticles, prior to the injection of the fluorescent silica microspheres.

2.4.1 Characterization of fluorescent silica microspheres

Fluorescent silica microspheres were characterized in terms of size and shape, zeta potential and light emission (fluorescence). The size and shape of the microspheres were characterized using an optical microscope and scanning electron microscope (SEM). Zeta potential was measured using Zetasizer manufactured by Malvern Instruments. The emission spectrum was obtained using Fluorescent Spectrometer manufactured by Horbia.

Three fluorescent silica microsphere samples (Figure 2.4) of different sizes and fluorescence colors were purchased from Corpuscular Inc., New York, USA. They were 1 μm blue, 4 μm green and 10 μm red fluorescent silica microspheres.



Figure 2.4: Picture of the blue, green, and red fluorescence silica microsphere samples purchased from Corpuscular Inc.

2.4.1.1 Blue microspheres

Optical imaging of the blue microspheres sample is shown in Figure 2.5. The blue sample was shown to have uniformly shaped spheres with an average particle size of about 2 μm . SEM imaging confirmed this measurement as shown in Figure 2.6.

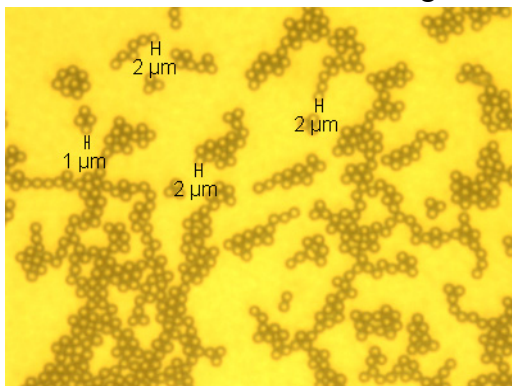


Figure 2.5: Optical image of the blue fluorescent silica microspheres.

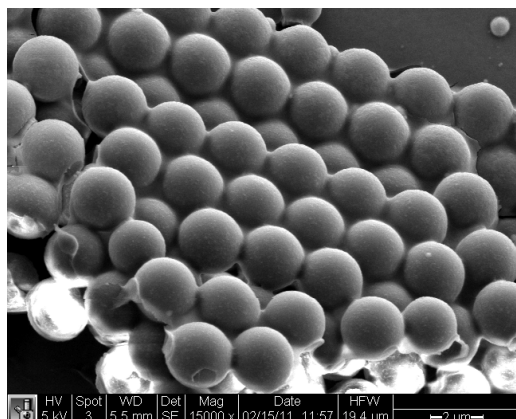


Figure 2.6: SEM image of the blue fluorescent silica microspheres.

The blue fluorescent silica sample volume was five cubic centimeters with concentration of five percent. The density of the sample was measured in the laboratory at temperature of 24.5°C. An accurate pipette was used to obtain one cubic centimeter of microfluid at original concentration. The weight of the one cubic centimeter sample was measured using a balance with one milligram accuracy. It was found that the density of the blue fluorescence silica microfluid sample was about 4.995×10^{-2} grams per cubic centimeter.

Following the concentration or density measurement, several dilutions were prepared. The microfluid was diluted one part of silica microfluid into 25, 50 and 100 parts of deionized water. The new concentrations of diluted samples are summarized in Table 2.2.

Table 2.2: Summary of diluted samples concentration of blue fluorescence silica sample.

Sample	Microfluid volume	Original concentration	Water volume	Diluted sample volume	Diluted sample concentration
	cm ³	g/cm ³	cm ³	cm ³	g/cm ³
1 to 100	0.02	4.995×10^{-2}	1.98	2	4.995×10^{-4}
1 to 50	0.04	4.995×10^{-2}	1.96	2	9.990×10^{-4}
1 to 25	0.08	4.995×10^{-2}	1.92	2	1.998×10^{-3}

The zeta potential of all diluted samples was measured. Each measurement was repeated four times for every sample. The average zeta potential of the most diluted sample (1:100) was found to be around positive 15.4 mV with standard deviation of 1.27. The average zeta potential of the second most diluted sample (1:50) was about positive 15.3 mV with standard deviation of 1.86. The average zeta potential of (1:25) diluted sample was around positive 53.6 mV with standard deviation of 0.8. The zeta potential of the (1:25) diluted sample was 72% higher than the more diluted (1:100 and 1:50) samples. This was attributed to the possible aggregation of the silica microspheres in which the measured zeta potential is in fact the charge of the whole aggregated particles, not the individual particle. The zeta potential distribution of all diluted samples is illustrated in Figure 2.7.

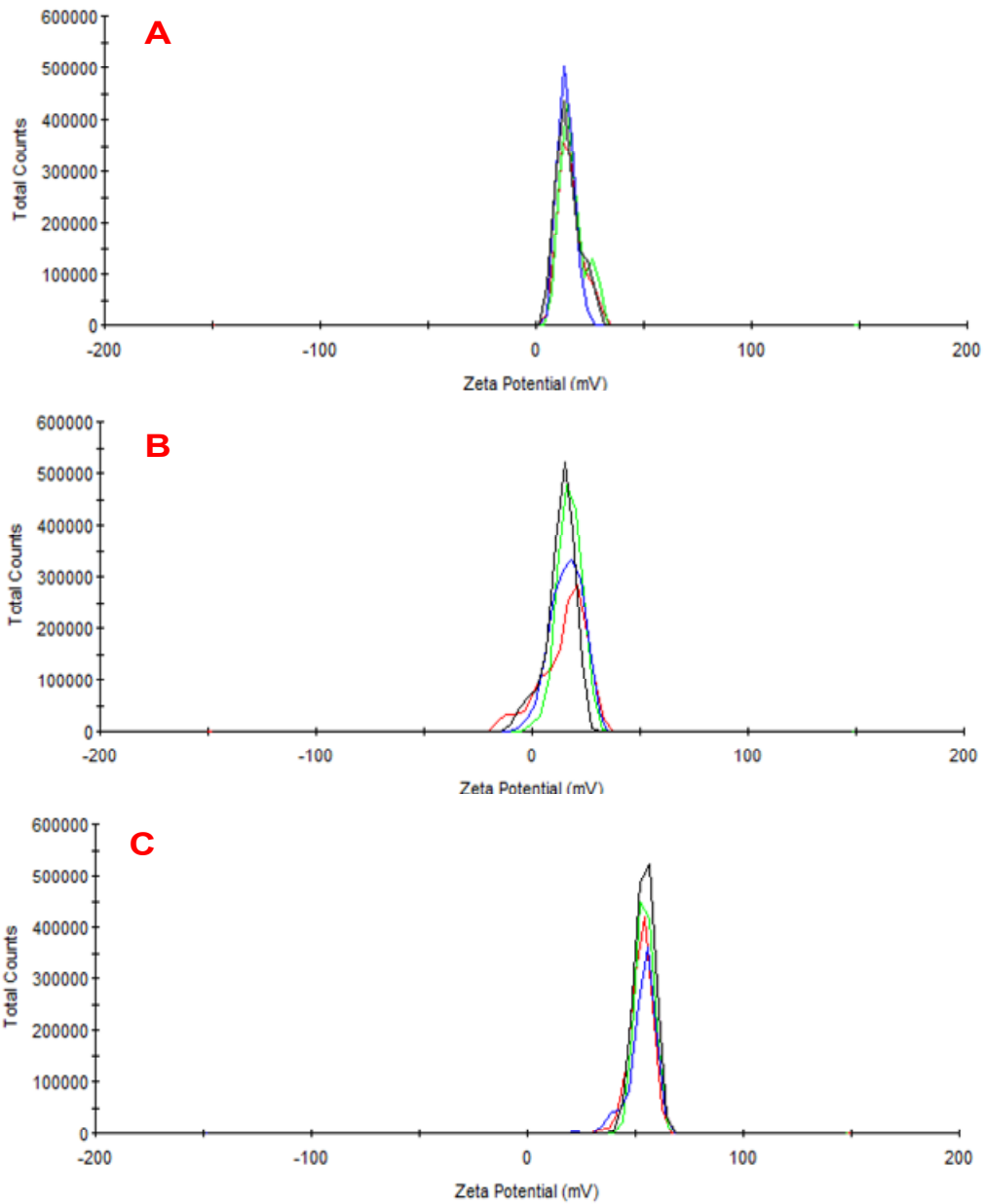


Figure 2.7: Zeta potential distribution of (A) 1:100, (B) 1:50 and (C) 1:25 diluted samples of the blue fluorescent silica microfluid.

A fluorescence spectrometer was used to measure the emission spectrum of the samples. The sample was excited at wavelength of 410 nm and the emission spectrum was measured (Figure 2.8) between 410 to 700 nm. The sample has a peak or maximum emission at wavelength of about 477 nm.

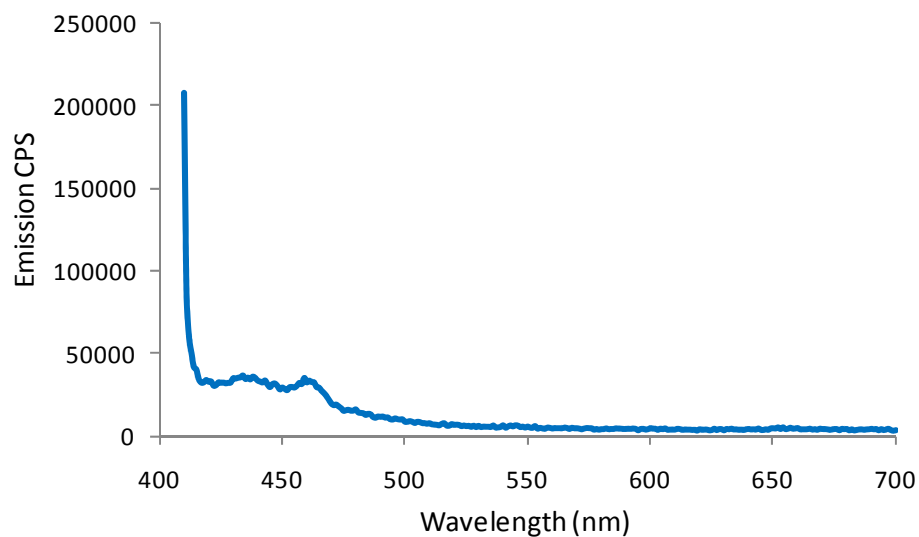


Figure 2.8: Emission spectrum of the blue fluorescent silica microsphere sample.

2.4.1.2 Green microspheres

Optical imaging of the green fluorescent silica microspheres sample is shown in Figure 2.9. The green sample has uniformly shaped spheres of an average particle size of about 5 μm . SEM imaging confirmed the size measurement and particle shape as shown in Figure 2.10.

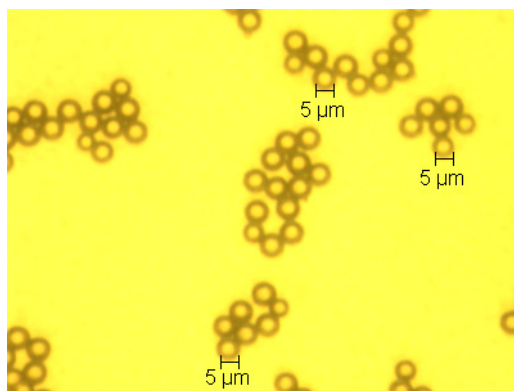


Figure 2.9: Optical image of the green fluorescent silica microspheres.

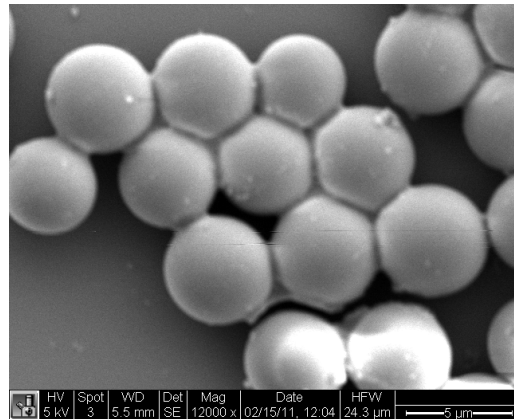


Figure 2.10: SEM image of the green fluorescent silica microspheres.

The volume and concentration of the original green and blue fluorescent silica microfluid samples were identical. The green sample volume was five cubic centimeters with concentration of five percent. The density of the sample was measured in the laboratory at a temperature of 24.5°C. An accurate pipette was used to obtain one cubic centimeter of microfluid at original concentration. The weight of the one cubic centimeter sample was measured using a balance with one milligram accuracy. It was found that the density of the green fluorescence silica microfluid sample was about 4.93×10^{-2} grams per cubic centimeters.

Following the concentration or density measurement, several dilutions were prepared. The microfluid was diluted one part of silica microfluid into 25, 50 and 100 parts of deionized water. The new concentrations of diluted samples are summarized in Table 2.3.

Table 2.3: Summary of diluted samples concentration of green fluorescence silica sample.

Sample	Microfluid volume	Original concentration	Water volume	Diluted sample volume	Diluted sample concentration
	cm ³	g/cm ³	cm ³	cm ³	g/cm ³
1 to 100	0.02	4.93×10^{-2}	1.98	2	4.93×10^{-4}
1 to 50	0.04	4.93×10^{-2}	1.96	2	9.86×10^{-4}
1 to 25	0.08	4.93×10^{-2}	1.92	2	1.97×10^{-3}

The zeta potential of all diluted samples was measured. Each measurement was repeated four times for every diluted sample. The average zeta potential of the most diluted sample (1:100) was found to be around negative 80.2 mV with standard deviation of 1.77. The average zeta potential of most concentrated sample (1:25 diluted sample) was around negative 72.5 mV, 9% less than the zeta potential measured on the (1:100) diluted sample. The average zeta potential of the (1:50) diluted sample was about positive 35.3 mV with standard deviation of 2.65. There was a significant shift in the average zeta potential between the (1:50) and other diluted samples (1:100 and 1:25). This might have resulted from the settlement of the silica microparticles at the bottom of the measurement cell during the analysis. The average size of green fluorescent silica microspheres was 5 μm.

Visual observation showed that particles of this size do not stay in suspension for more than a few minutes. The zeta potential distribution of all diluted samples is illustrated in Figure 2.11.

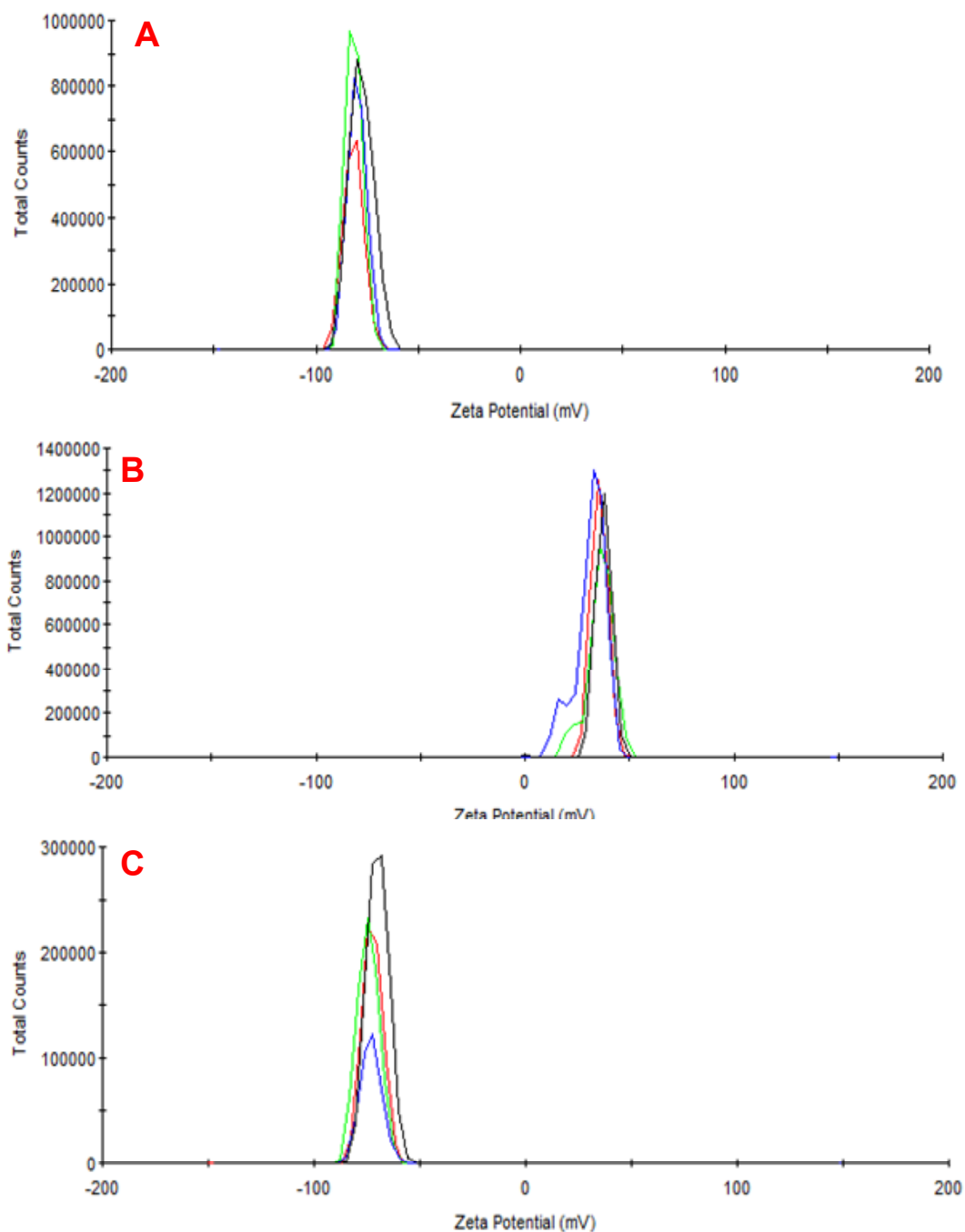


Figure 2.11: Zeta potential distribution of (A) 1:100, (B) 1:50 and (C) 1:25 diluted samples of the green fluorescent silica microfluid

The emission spectrum of the green fluorescent silica microsphere sample was measured (Figure 2.12). The sample was excited at wavelength of 410 nm and the emission spectrum was measured between 410 to 750 nm. The sample has a peak or maximum emission at wavelength of about 540 nm.

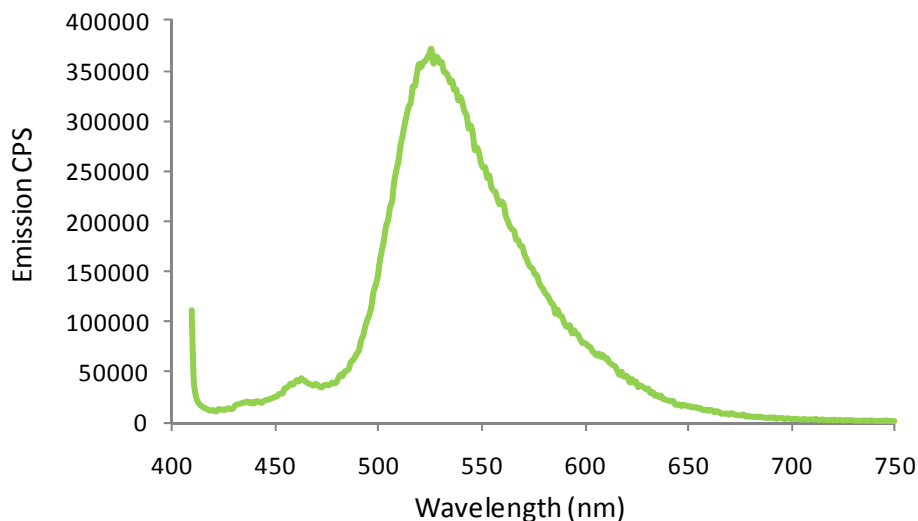


Figure 2.12: Emission spectrum of the green fluorescent silica microsphere sample.

2.4.1.3 Red microspheres

Optical imaging of the red fluorescent silica microspheres sample is shown in Figure 2.13. The red sample has uniformly shaped spheres. The silica spheres were polydisperse or polysized. The sample has spheres with diameters ranging from 5 to 26 μm . SEM imaging confirmed the size measurement and particle shape as shown in Figure 2.14.

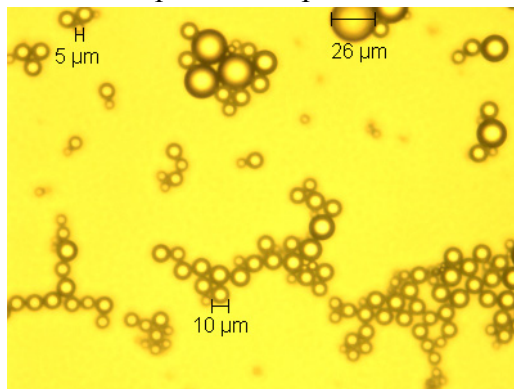


Figure 2.13: Optical image of the red fluorescent silica microspheres.

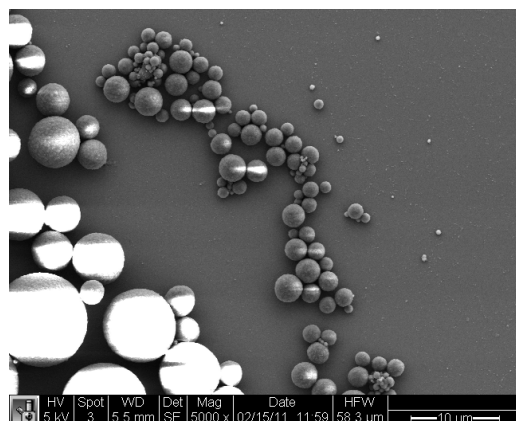


Figure 2.14: SEM image of the red fluorescent silica microspheres.

The emission spectrum of the red fluorescent silica microsphere sample was measured (Figure 2.15). The sample was excited at wavelength of 410 nm and the emission spectrum was measured between 430 to 800 nm. The sample has multiple peaks or maximum emissions at wavelengths of about 488 and 577 nm.

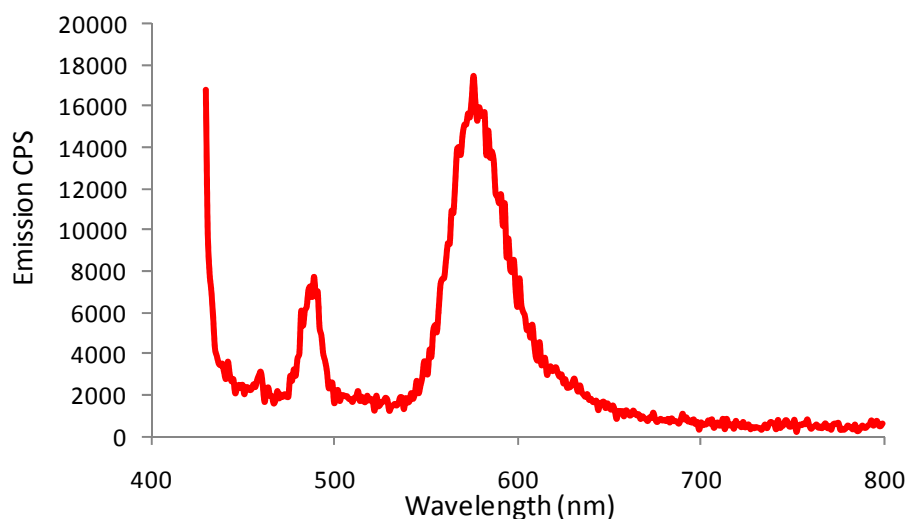


Figure 2.15: Emission spectrum of the red fluorescence silica microsphere sample.

The polydispersity disqualified the red fluorescent silica sample from being suitable for the injection experiments and therefore no further characterization was conducted.

2.4.2 Characterization of silicon dioxide (SiO₂) nanoparticles

The silicon dioxide (SiO₂) nanoparticles were characterized in terms of size, size distribution and zeta potential using SEM, Dynamic Light Scattering (DLS) and Zetasizer, respectively. The SiO₂ had average size of about 350 nm as shown in the SEM image in Figure 2.16.

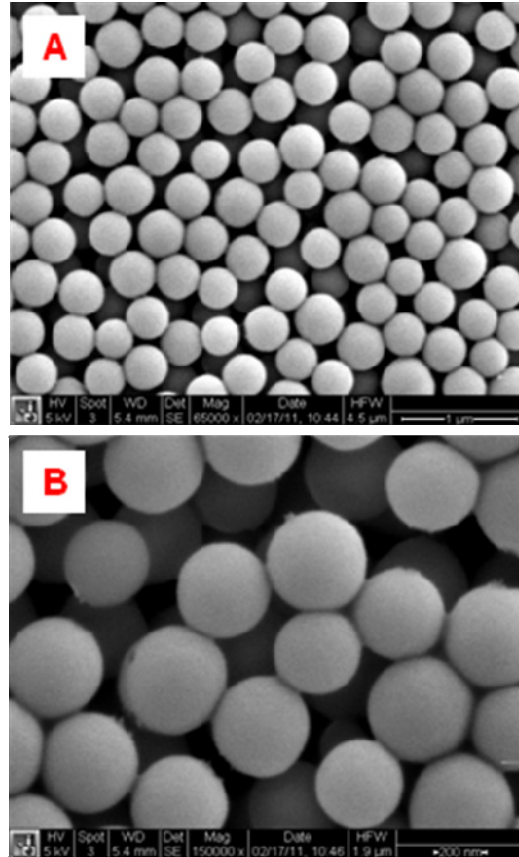


Figure 2.16: SEM image of the silicon dioxide nanoparticles in the influent.

The size distribution of the silicon dioxide nanofluid sample (Figure 2.17) obtained from DLS also showed that the sample has an average particle size of about 350 nm.

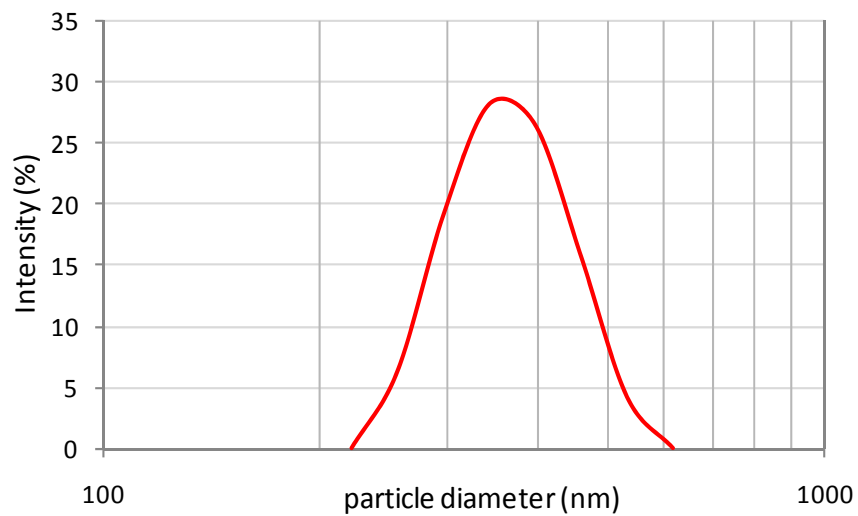


Figure 2.17: Particle size distribution by light intensity percentage of the influent.

The zeta potential of the silicon dioxide nanoparticle sample was measured and the average of two sets of measurement was found to be negative 73.4 mV with standard deviation of 1.77. The zeta potential distribution of both measurements is shown in Figure 2.18. The fractured greywacke core sample carries a negative charge. So it is of interest to inject particles that carry the same type of charge (i.e. negative charge), as similar charges repel and should prevent particle attachment to the core.

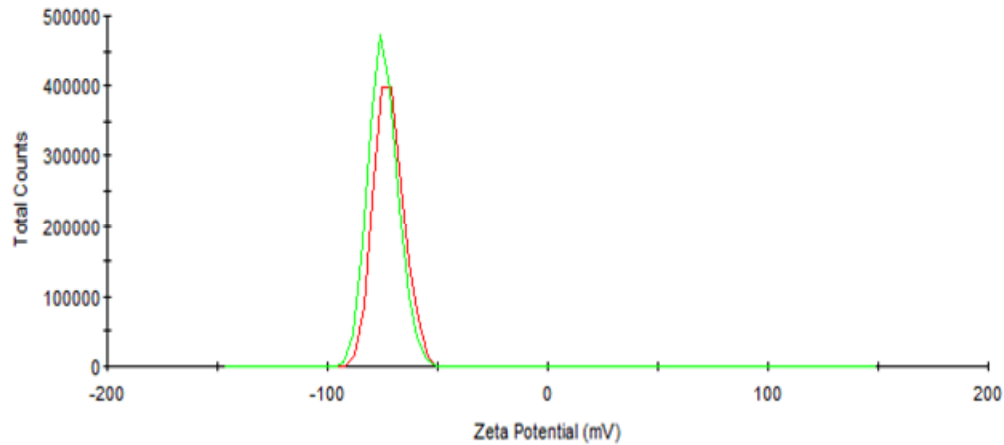


Figure 2.18: Zeta potential distribution of silicon dioxide nanoparticles.

2.4.3 Silicon dioxide (SiO₂) nanoparticle injection into fractured greywacke

The silicon dioxide nanoparticles injection was conducted to investigate their flow through the fractured greywacke core sample. The testing apparatus was similar to the permeability measurement experiment, but modified slightly to allow for the injection of nanoparticles. The configuration also allows for injection of particle-free deionized water, without interrupting the flow. The modified apparatus can be seen in Figure 2.19.

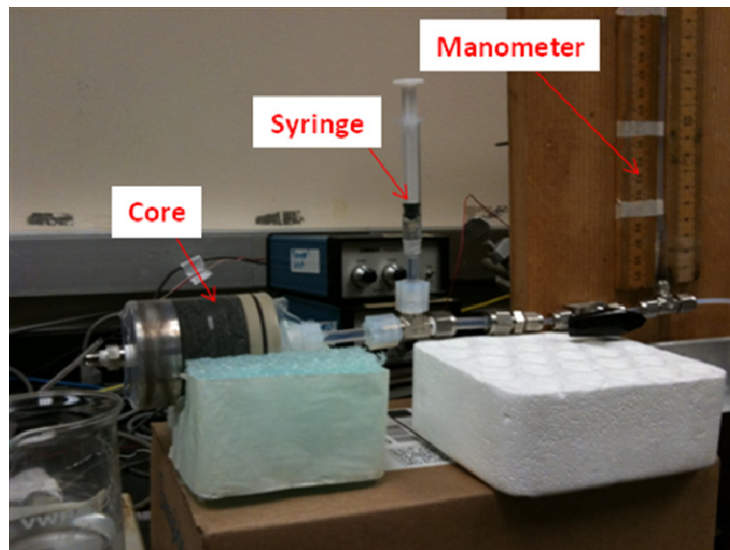


Figure 2.19: A picture of the silicon dioxide nanoparticle injection apparatus.

The nanofluid was contained in a syringe downstream the water pump. The silicon dioxide nanoparticles were injected using the syringe. The nanofluid of unknown concentration was diluted one part to 50 parts of deionized water. The volume injected into the core sample is one cubic centimeter. Prior to the injection of the nanofluid, the core was preflushed with several pore volumes of deionized water to displace rock fines and debris. Following the injection of the nanofluid (1 cm^3), a continuous flow of deionized water was introduced. Specifically, eight pore volumes of water were injected. The core was then backflushed with three pore volumes to flush any trapped particles at the inlet side of the core. The average flow rate during the injection was about $0.1 \text{ cm}^3/\text{min}$ at an inlet pressure of about 0.1 atm. A total of ten effluent samples was collected and analyzed using SEM and DLS.

2.5 RESULTS

This section provides the results of the injection of silicon dioxide nanoparticles into the fractured greywacke core. The objective of this experiment was to investigate the transport of silicon dioxide nanoparticles through fractured greywacke core, providing a baseline for subsequent injections of the fluorescent silica microspheres.

The silicon dioxide (SiO_2) nanoparticles flowed through the fractured greywacke core successfully. The nanoparticles had a relatively narrow distribution of size between 350 – 420 nanometers (Figure 2.17). The nanoparticles were easily distinguishable from the core fines and debris due to their size and spherical shape, even though all are made of same material as the rock itself (silica). The effluent samples were examined for the presence of the nanoparticles using the DLS technique. For instance, the effluent samples at the second and third post-injected pore volumes of deionized water showed particle size distributions that were identical to the particle size distribution of the injected influent. The particle size distributions of these effluent samples is shown in Figure 2.20.

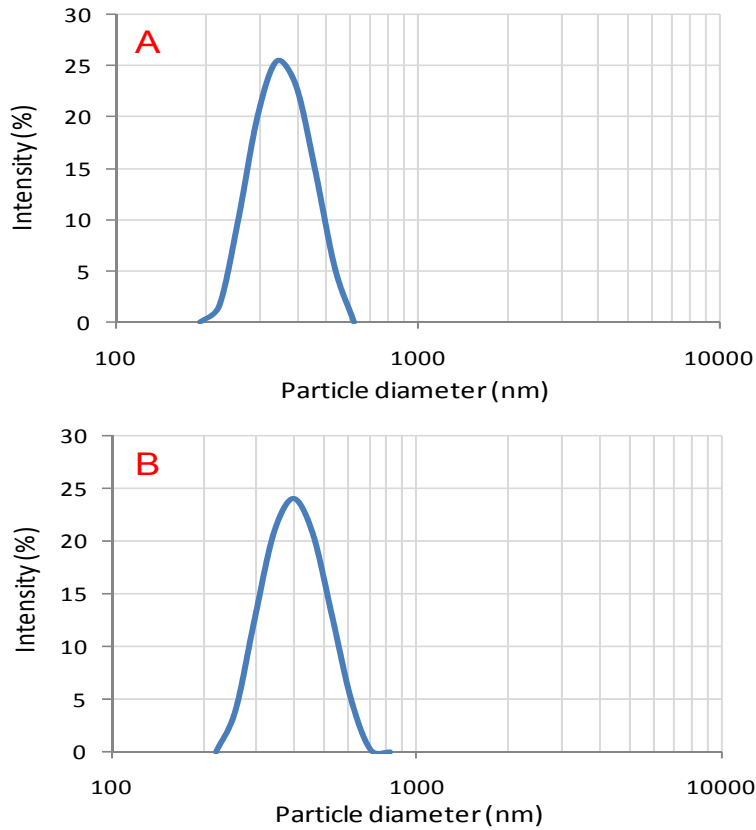


Figure 2.20: Particle size distribution by intensity percentage of effluent samples at (A) second and (B) third post-injected pore volume of deionized water.

The more precise approach using SEM imaging of the effluent confirmed this finding (Figure 2.21). The average nanoparticle size in Figure 2.21 is around 350 nanometers.

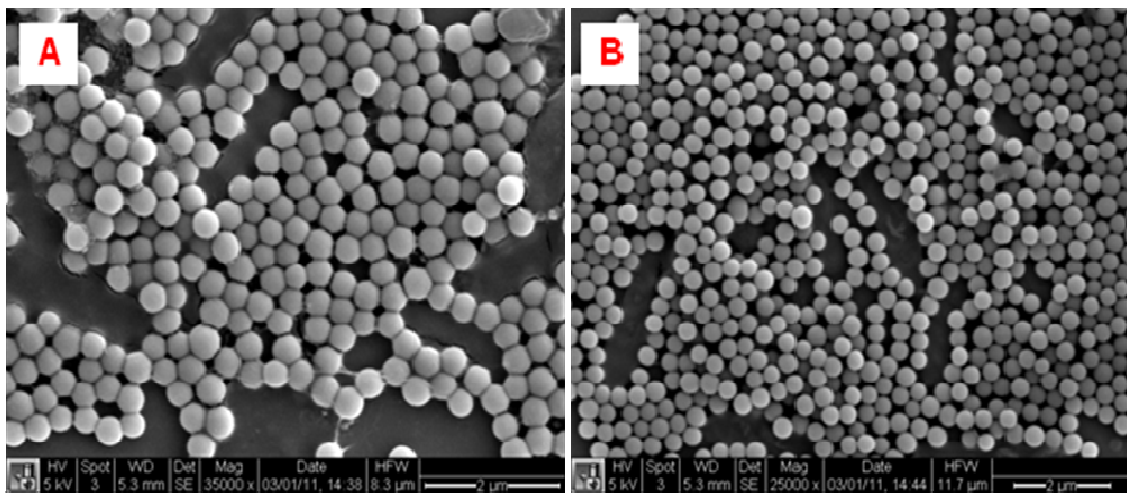


Figure 2.21: SEM image showing SiO_2 nanoparticles in the effluent samples at (A) second and (B) third post-injected pore volume of deionized water.

SEM imaging of an effluent sample at the seventh post-injected pore volume showed the decrease in the silicon dioxide nanoparticles as more water was injected (Figure 2.22). Only few nanoparticles were identified in the later effluent sample.

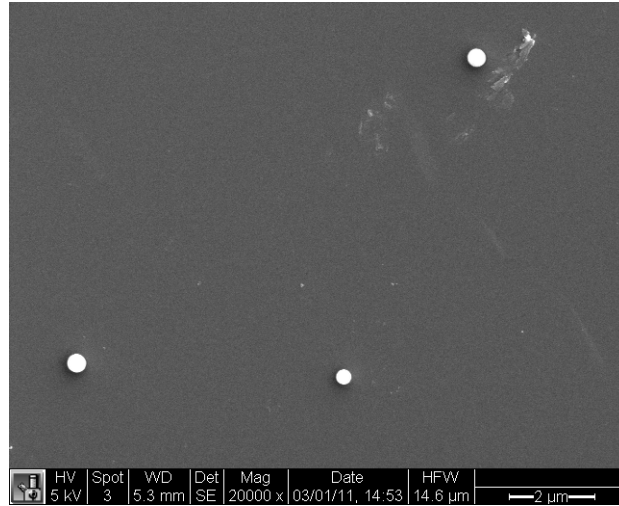


Figure 2.22: SEM image showing few SiO₂ nanoparticles in the effluent sample at later post-injected pore volume of deionized water.

The permeability measurement (Figure 2.23) during and after the injection of the SiO₂ nanofluid was relatively constant with minimal change of about ± 3 darcy. Note that the permeability during the post-injection was about 47 darcy, 22% less than the permeability values measured right after saturation of the core sample. This was believed to be caused by the swelling of the clays of core. A significant reduction in permeability during the backflushing of the core sample was observed. There was approximately 86% reduction in the permeability from 47 to 7 darcy. It is worth mentioning that the backflushing of the sample was conducted a few weeks after the injection of the nanoparticles. By that time, the core had been saturated for about 2 months. It is not unexpected that the clays in the core could be swelling, especially as greywacke is known to have a high content of clay materials. Consequently, the injection of the fluorescent silica microsphere was postponed. The core will be dried and resaturated with deionized water. The injection of silicon dioxide nanoparticles will be repeated, followed immediately by the fluorescent silica microspheres. This should reduce the possibility of clay swelling at least prior to the injection of the silica microspheres.

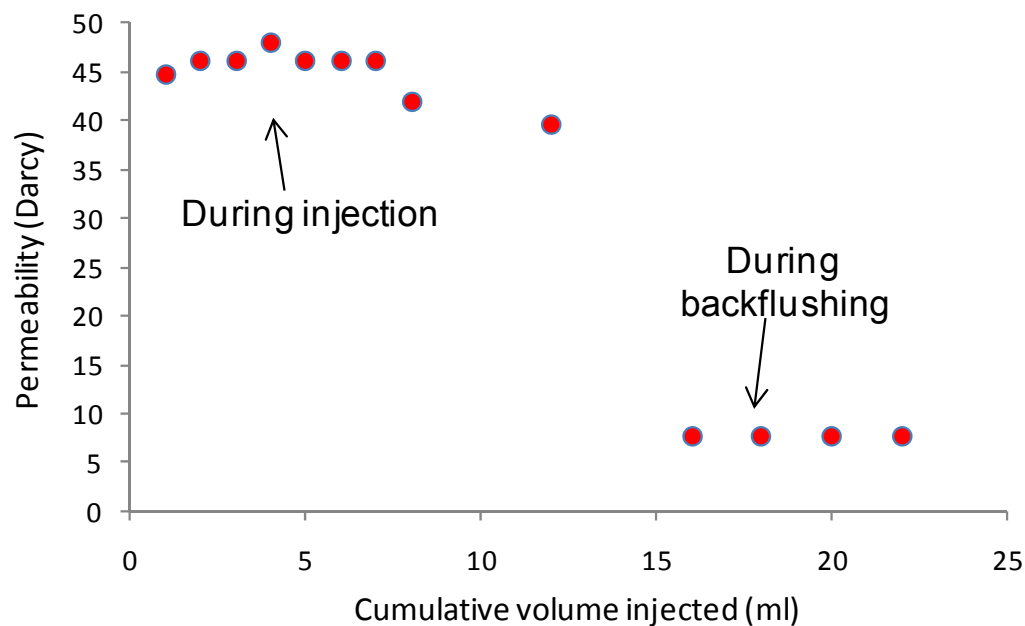


Figure 2.23: Permeability measurements during injection and backflushing of the fractured greywacke core sample.

2.6 SYNTHESIS AND CHARACTERIZATION OF TIN-BISMUTH NANOPARTICLES

In the tin-bismuth injection experiment performed last quarter (Oct. – Dec., 2010), it was found that only particles with diameters of 200 nm and smaller were transported successfully through the pore spaces of the Berea sandstone core. Thus, it is desired to obtain a sample of tin-bismuth alloy nanoparticles that has a narrow size distribution and contains particles smaller than 200 nm. This would allow a more conclusive demonstration of the particle growth temperature-sensing mechanism and may aid particle transport through rock. To this end, the sample of tin-bismuth nanoparticles that was synthesized last quarter was centrifuged at various speeds, and characterized using DLS. While encouraging results were obtained, the resulting sample still contained particles larger than 200 nm and was very dilute. For this reason, the sonochemical synthesis and subsequent cleaning of tin-bismuth nanoparticles was repeated at the highest possible sonication power for the type of mineral oil used. This sample was centrifuged, and the original and resulting samples were characterized using DLS.

2.6.1 Centrifugation and characterization

The tin-bismuth alloy nanoparticles were characterized in terms of size using DLS (Figure 2.20). This sample was centrifuged at 1000 rpm for 15 minutes, and the supernatant was characterized using DLS (Figure 2.20). Subsequently, the supernatant from the first centrifugation was centrifuged at 2500 rpm for 20 minutes, and the supernatant from this second centrifugation was characterized using DLS (Figure 2.24).

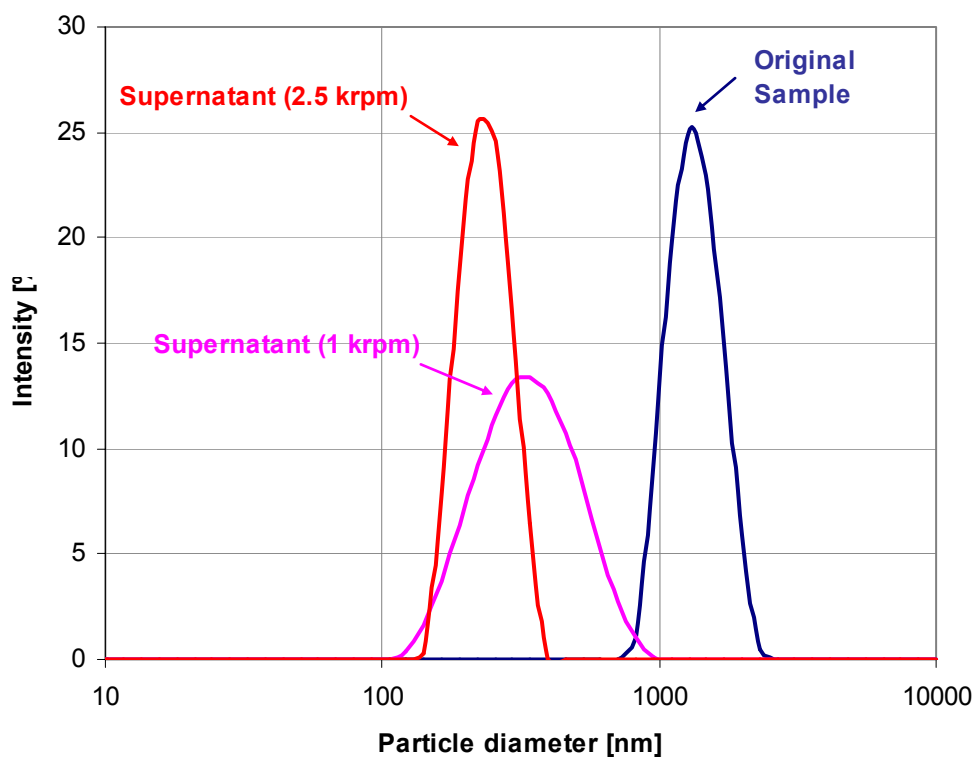


Figure 2.24: Particle size distribution by light intensity percentage of original sample and supernatant samples of tin-bismuth alloy nanoparticles

It is shown in Figure 2.24 that the size distribution was narrowed significantly by centrifugation, and the peak particle diameter was lowered from to 1370 nm (original sample) to 360 nm (1000 rpm), and, subsequently, 239 nm (2500 rpm). However, the final sample after centrifuging at 2500 rpm appeared by visual inspection to be very dilute. Also, judging from these DLS results, there are still particles larger than 200 nm in the sample. Chen et al. (2005) reported that higher sonication power used during synthesis leads to smaller diameter particles and tighter size distributions. Thus, it was decided to repeat the synthesis at higher sonication power.

2.6.2 Synthesis of tin-bismuth alloy nanoparticles

To perform the synthesis, Sn and Bi were melted together at the eutectic composition (~60 wt % Bi and ~40 wt % Sn). After the alloy was cooled to room temperature, a 0.98 g sample was sonicated in 120 ml of light paraffin oil, a slight variation of the sonochemical method suggested by Chen et al. (2005). The VC-750 ultrasonic processor manufactured by Sonics & Materials, Inc. with a 0.75 in. diameter high gain solid probe was used. The sonicator was operated at 90% amplitude (with a splash guard constructed of Teflon tape to prevent loss of the sample), resulting in an average ultrasonic power of 145 W. The mixture was cooled to room temperature. The alloy particles were washed and centrifuged twice with a 1:1 mixture of acetone and hexane, once with a 3:1 mixture of acetone and

hexane, once in a solution of 0.1 M polyvinyl pyrrolidone (PVP) in ethanol, and once in ethanol. After this final wash and centrifuge, the nanoparticles were suspended in water. The centrifuge setting was 6000 rpm for 15 minutes each time.

2.6.3 Centrifugation and characterization of new sample

This latest sample of tin-bismuth alloy nanoparticles was characterized in terms of size using DLS (Figure 2.25). This sample was centrifuged at 2500 rpm for 30 minutes, and both the supernatant and infranatant were characterized using DLS (Figure 2.25).

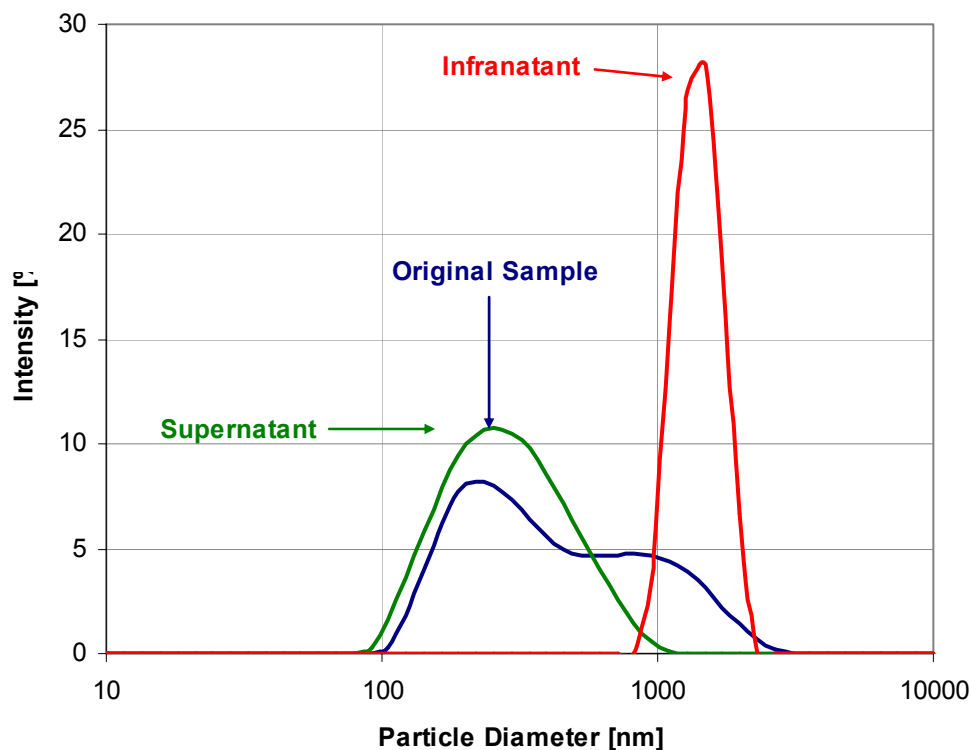


Figure 2.25: Particle size distribution by light intensity percentage of original tin-bismuth alloy nanoparticles and separated samples after centrifugation at 2500 rpm for 30 min.

By comparison of Figures 2.24 and 2.25, it can be seen that the original sample of this latest synthesis had a higher fraction of smaller particles, as predicted. This sample was found to have a bimodal distribution with peaks at 306 nm and 1087 nm. After centrifugation, this sample was separated into a supernatant with a peak at 318 nm and an infranatant with a peak at 1430 nm. These results suggest that the incremental centrifugation performed with the previous sample was a more effective method of separation.

2.7 FUTURE WORK

The next stage will be to dry and resaturate the fractured greywacke core sample. The injection of silicon dioxide nanoparticles will be repeated. The fluorescent silica microspheres will be injected immediately after the injection of the silica nanoparticles to avoid swelling of the clays before the microspheres injection. Microspheres of different sizes and colors will be injected through the fracture and effluent samples will be collected. Fracture properties such as size and shape may be inferred from the production history of those microspheres.

The tin-bismuth nanoparticle samples described in this report will be characterized using SEM in order to verify or refute DLS results. Filtration will be investigated as another means of separation by particle size. When a sufficiently monodisperse sample of tin-bismuth nanoparticles with diameters less than 200 nm is obtained, further heating experiments, flow experiments, and combined heat and flow experiments will be performed. Finally, the feasibility of the magnetic collection of nanoparticles will be investigated.

3. FRACTURE CHARACTERIZATION USING RESISTIVITY

This research project is being conducted by Research Assistant Lilja Magnúsdóttir, Senior Research Engineer Kewen Li and Professor Roland Horne. The objective is to investigate ways to use resistivity to infer fracture properties in geothermal reservoirs.

3.1 SUMMARY

The aim of this project is to use resistivity measurements and modeling to characterize fracture properties in geothermal fields. The resistivity distribution in the field can be estimated by measuring potential differences between various points and the resistivity data can be used to infer fracture properties due to the large contrast in resistivity between water and rock.

In previous work, a two-dimensional model has been developed to calculate a potential field due to point sources of excitation. The model takes into account heterogeneity by solving the potential field for inhomogeneous resistivity. Fractures are modeled as areas with resistivity different from the rock, to investigate the changes in the potential field around them. The grid is rectangular and nonuniform so the fracture elements can be modeled smaller than the elements for the rest of the reservoir, in order to decrease the total number of elements. Flow simulations have been performed of a conductive fluid injected into a reservoir to enhance the difference in resistivity between fractures and rock, and the potential difference has been calculated between two wells as a function of time as the fluid flows through the fractured rock. These previous results for simple fracture networks showed that the time history of voltage differences correspond to the fracture networks and therefore have shown promising possibilities in indicating fracture locations and character.

An attempt has been made to use flow simulator TOUGH2 instead of previously described resistivity model to solve the electrical field. The approach is believed to be possible because of the analogy between Ohm's law that describes electrical flow and Darcy's law describing fluid flow. By using TOUGH2 to solve the electrical field, the same grid can be used to solve the flow of a conductive fluid through the network and the corresponding electric potential. TOUGH2 allows the use of nonrectangular elements making it easier to model complicated fracture patterns with fewer elements. The simulation is therefore more efficient and faster when TOUGH2 is used instead of the previously developed resistivity model.

Future work includes studying further the relationship between fracture networks and the change in potential differences as conductive tracer is injected into the reservoir for more complicated fractal network of fractures. Another future goal is to study the possibility of using the potential differences with inverse modeling to characterize fracture patterns.

3.2 INTRODUCTION

In an Enhanced Geothermal System (EGS) application, the configuration of the fractures is central to the performance of the system. Therefore fracture characterization is important

to design the recovery strategy appropriately and thereby to optimize the overall efficiency of geothermal energy recovery.

The goal of this study is to find ways to use Electrical Resistivity Tomography (ERT) to characterize fractures in geothermal reservoirs. ERT is a technique for imaging the resistivity of a subsurface from electrical measurements. Pritchett (2004) concluded based on a theoretical study that hidden geothermal resources can be explored by electrical resistivity surveys because geothermal reservoirs are usually characterized by substantially reduced electrical resistivity relative to their surroundings. Electrical current moving through the reservoir passes mainly through fluid-filled fractures and pore spaces because the rock itself is normally a good insulator. In these surveys, a direct current is sent into the ground through electrodes and the voltage differences between them are recorded. The input current and measured voltage difference give information about the subsurface resistivity, which can then be used to infer fracture locations.

Resistivity measurements have been used in the medical industry to image the internal conductivity of the human body, for example to monitor epilepsy, strokes and lung functions as discussed by Holder (2004). In Iceland, ERT methods have been used to map geothermal reservoirs. Arnarson (2001) describes how different resistivity measurements have been used effectively to locate high temperature fields by using electrodes located on the ground's surface. Stacey et al. (2006) investigated the feasibility of using resistivity to measure saturation in a rock core. A direct current pulse was applied through electrodes attached in rings around a sandstone core and it resulted in data that could be used to infer the resistivity distribution and thereby the saturation distribution in the core. It was also concluded by Wang and Horne (2000) that resistivity data have high resolution power in the depth direction and are capable of sensing the areal heterogeneity.

In the approach considered in this project so far, electrodes would be placed inside two geothermal wells (future work will involve studying different electrode arrangements with a greater number of wells) and the potential differences between them studied to locate fractures and infer their properties. Due to the limited number of measurement points, the study is investigating ways to enhance the process of characterizing fractures from sparse resistivity data. For example, in order to enhance the contrast in resistivity between the rock and fracture zones, a conductive tracer would be injected into the reservoir and the time-dependent voltage difference measured as the tracer distributes through the fracture network.

Slater et al. (2000) have shown a possible way of using Electrical Resistivity Tomography (ERT) with a tracer injection by observing tracer migration through a sand/clay sequence in an experimental $10 \times 10 \times 3 \text{ m}^3$ tank with cross-borehole electrical imaging. Singha and Gorelick (2005) also used cross-well electrical imaging to monitor migration of a saline tracer in a $10 \times 14 \times 35 \text{ m}^3$ tank. In previous work, usually many electrodes were used to obtain the resistivity distribution for the whole field at each time step. The resistivity distribution was then compared to the background distribution (without any tracer) to see resistivity changes in each block visually, to locate the saline tracer and thereby the

fractures. Using this method for a whole reservoir would require a gigantic parameter space, and the inverse problem would not likely be solvable, except at very low resolution. However, in the method considered in this study, the potential difference between the wells would be measured and plotted as a function of time while the conductive tracer flows through the fracture network. Future work will involve using that response, i.e. potential difference vs. time, in an inverse modeling process to characterize the fracture pattern.

First, the theory behind previously developed resistivity model is defined and previous work described where the potential differences were calculated for two cases while a conductive fluid was injected into the reservoir, in order to show the difference in electrical potential time history between these two cases. Then, the analogy between water flow and electrical flow is described and the electrical field is calculated using the resistivity model as well as TOUGH2 flow simulator to explore the possibility of making TOUGH2 solve the electrical potential. That would allow the use of nonrectangular elements since the same grid could be used for the flow simulation of the conductive tracer and the calculations of the electrical field, making the simulations faster and more efficient. Finally, future work is outlined.

3.3 RESISTIVITY MODEL

One of the main problems in resistivity modeling is to solve the Poisson equation that describes the potential field and to complete the inversion iteration efficiently. That governing equation can be derived from basic electrical relationships as described by Dey and Morrison (1979). Ohm's Law defines the relationship between current density, J , conductivity of the medium, σ , and the electric field, E , as

$$J = \sigma E \quad (3.1)$$

The stationary electric fields are conservative, so the electric field at a point is equal to the negative gradient of the electric potential there, i.e.

$$E = -\nabla \phi \quad (3.2)$$

where ϕ is the scalar field representing the electric potential at the given point. Hence,

$$J = -\sigma \nabla \phi \quad (3.3)$$

Current density is the movement of charge density, so according to the continuity equation, the divergence of the current density is equal to the rate of change of charge density,

$$\nabla J = \frac{\partial Q(x, y, z)}{\partial t} = q(x, y, z) \quad (3.4)$$

where q is the current density in amp m^{-3} . Combining Equations (3.3) and (3.4) gives the following Poisson equation which describes the potential distribution due to a point source of excitation,

$$\nabla[\sigma \nabla \phi] = -q(x, y, z) \quad (3.5)$$

The conductivity σ is in mhos m^{-1} and the electric potential is in volts. This partial differential equation can then be solved numerically for the resistivity problem.

3.3.1 Finite Difference Equations in Two Dimensions

The finite difference method is used to approximate the solution to the partial differential Equation (3.5) using a point-discretization of the subsurface (Mufti, 1976). The

computational domain is discretized into $N_x \times N_y$ blocks and the distance between two adjacent points on each block is h in x-direction and l in y-direction, as shown in Figure 3.1.

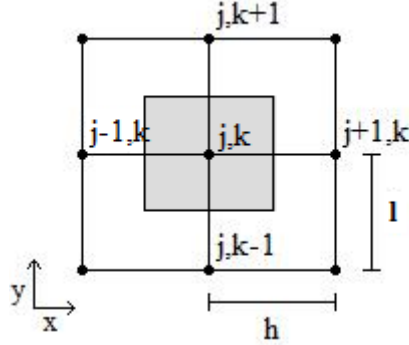


Figure 3.1: Computational domain, discretized into blocks.

Taylor series expansion is used to approximate the derivatives of Equation (3.5) about a point (j,k) on the grid,

$$\left. \frac{\partial}{\partial x} \left(\sigma \frac{\partial \phi}{\partial x} \right) \right|_{(j,k)} \approx \frac{\left[\begin{array}{l} \phi(j+1,k)\sigma\left(j+\frac{1}{2},k\right) + \phi(j-1,k)\sigma\left(j-\frac{1}{2},k\right) \\ - \left[\sigma\left(j+\frac{1}{2},k\right)\sigma\left(j-\frac{1}{2},k\right) \right] \phi(j,k) \end{array} \right]}{h^2} \quad (3.6)$$

$$\left. \frac{\partial}{\partial y} \left(\sigma \frac{\partial \phi}{\partial y} \right) \right|_{(j,k)} \approx \frac{\left[\begin{array}{l} \phi(j,k+1)\sigma\left(j,k+\frac{1}{2}\right) + \phi(j,k-1)\sigma\left(j,k-\frac{1}{2}\right) \\ - \left[\sigma\left(j,k+\frac{1}{2}\right)\sigma\left(j,k-\frac{1}{2}\right) \right] \phi(j,k) \end{array} \right]}{l^2} \quad (3.7)$$

The point (j,k) represents the shaded area in Figure 3.1 (area = hl) so the current density due to an electrode at that point is given by,

$$q(j,k) = \frac{I}{hl} \quad (3.8)$$

where I [amp] is the current injected at point (j,k) Combining Equations (3.5)-(3.8) and solving for the electric potential ϕ at point (j,k) gives,

$$\phi(j,k) = \frac{[Ihl + \phi(j+1,k)c_1l^2 + \phi(j-1,k)c_2l^2 + \phi(j,k+1)c_3h^2 + \phi(j,k-1)c_4h^2]}{[c_1 + c_2]l^2 + [c_3 + c_4]h^2} \quad (3.9)$$

The parameters c_i represent the conductivity averaged between two adjacent blocks, i.e.

$$c_1 = \frac{2}{\rho(j,k) + \rho(j+1,k)} \quad (3.10)$$

$$c_2 = \frac{2}{\rho(j,k) + \rho(j-1,k)} \quad (3.11)$$

$$c_3 = \frac{2}{\rho(j,k) + \rho(j,k+1)} \quad (3.12)$$

$$c_4 = \frac{2}{\rho(j,k) + \rho(j,k-1)} \quad (3.13)$$

where $\rho(j,k)$ is the resistivity [ohm-m] of the node at grid coordinates j,k .

3.3.2 Iteration method

In order to solve Equation (3.9) numerically and obtain the results for electrical potential ϕ at each point on the grid, the iteration method called Successive Over-Relaxation was used (Spencer and Ware, 2009). At first, a guess is made for $\phi(j,k)$ across the whole grid, for example $\phi(j,k)=0$ for all j,k . That guess is then used to calculate the right hand side of Equation (3.9) (Rhs) for each point and the new set of values for $\phi(j,k)$ is calculated using the following iteration scheme,

$$\phi_{n+1} = \omega Rhs + (1 - \omega)\phi_n \quad (3.14)$$

The multiplier ω is used to shift the eigenvalues so the iteration converges better than simple relaxation. The number ω is between 1 and 2, and when the computing region is rectangular the following equation can be used to get a reasonable good value for ω ,

$$\omega = \frac{2}{1 + \sqrt{1 - R^2}} \quad (3.15)$$

where

$$R = \frac{\left(\cos\left(\frac{\pi}{Nx}\right) + \cos\left(\frac{\pi}{Ny}\right) \right)}{2} \quad (3.16)$$

The natural Neumann boundary condition is used on the outer boundaries, i.e. $\frac{\partial \phi}{\partial n} = 0$.

3.4 TIME HISTORY OF POTENTIAL DIFFERENCE

A flow simulation was performed using TOUGH2 reservoir simulator to see how a tracer, which increases the conductivity of the fluid, distributes after being injected into the reservoir. The simulation was carried out on a two-dimensional grid with dimensions $1000 \times 1000 \times 10 \text{ m}^3$ with fractured rock modeled as a squared area (green blocks), first in the lower right corner as shown in Figure 3.2, and then in the upper left corner as shown in Figure 3.3.

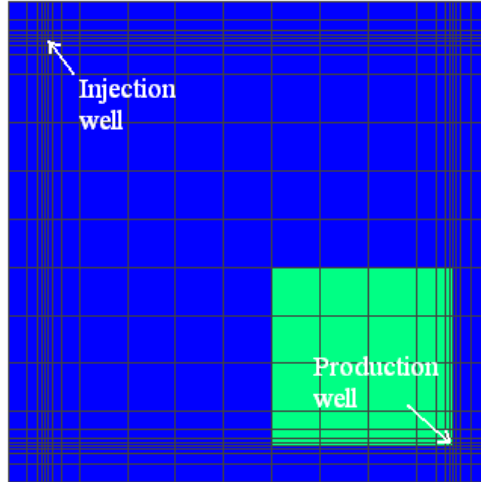


Figure 3.2: Fractured rock (green blocks) modeled in the lower right corner of the reservoir.

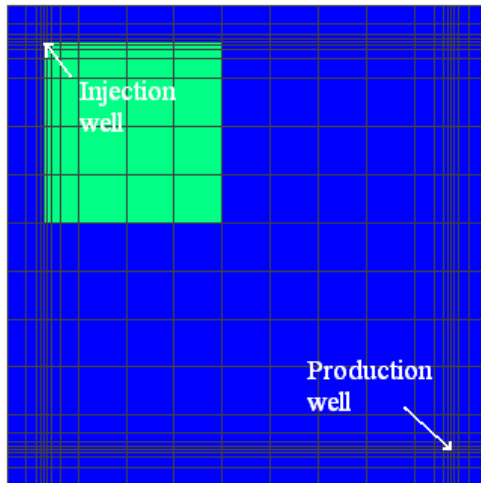


Figure 3.3: Fractured rock (green blocks) modeled in the upper left corner of the reservoir.

The goal was to study the difference in potential field between these two cases as conductive fluid is injected into the reservoir. The reservoir is modeled with porosity 0.4 and permeability 10^5 md (10^{-10} m²) while the fractured rock has porosity 0.65 and permeability 5×10^{10} md (5×10^{-5} m²).

No-flow boundary conditions were used and 100 kg/s of water was injected in the upper left corner with enthalpy 100 kJ/kg, and 0.1 kg/s of tracer with enthalpy 100 kJ/kg. The production well was set to produce at a constant pressure, 8 bar. The initial pressure was set to 9.6 bar, temperature to 150°C and initial tracer mass fraction to 10^{-9} because the simulator could not solve the problem with zero initial tracer mass fraction.

The following equation was used to calculate the electrical conductivity, $1/\rho_w$, of a NaCl water solution (Crain, 2010),

$$\rho_w = \frac{400,000}{\left(\frac{9}{5}T + 32\right)W_s} \quad (3.17)$$

in order to define conductivity values in the resistivity model as NaCl tracer flows through the reservoir. T is the formation temperature (assumed to be 150°C) and W_s is the water salinity [ppm NaCl].

The resistivity for the rock before fluid had been injected was set as 100 Ωm for the fractured area (assuming fractures were filled with water) and as 2000 Ωm for the rest of the reservoir. Figures 3.4 and 3.5 show how the potential difference between the injector and the producer changes with time for the reservoirs shown in Figure 3.2 and 3.3.

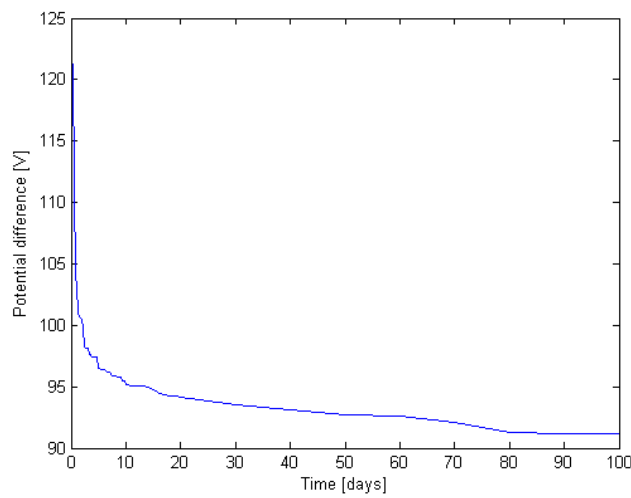


Figure 3.4: Potential difference between injection and production wells for reservoir in Figure 3.2.

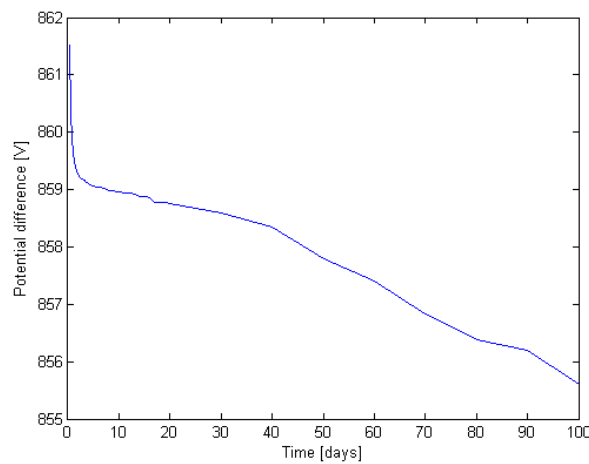


Figure 3.5: Potential difference between injection and production wells for reservoir in Figure 3.3.

The potential difference in the graph in Figure 3.4 drops very rapidly for the first 10 days, but then decreases more slowly when the tracer front has reached the fractured area. In Figure 3.5, the potential difference drops more slowly, as the conductive fluid first fills up the fractured rock, modeled with much higher porosity than the rest of the reservoir. More cases need to be studied, and probably run for a longer time period, in order to understand the correspondence between the changes in potential differences and fracture networks. But these preliminary results indicate that different fracture properties give different potential difference histories between two wells, and could therefore be used to indicate fracture characteristics.

3.5 WATER FLOW ANALOGY OF ELECTRICAL FLOW

The steady-state flow of an electric current through a conducting medium due to differences in energy potential is analogous to the steady-state flow of a fluid through porous medium. Darcy's law is an empirical relationship similar to Ohm's law (Equation 3.3) but instead of describing electrical flow it describes fluid flow through a porous medium,

$$q = -K\nabla h \quad (3.18)$$

where q is the flow rate [m/s], h is the head in meters and K is the hydraulic conductivity given by,

$$K = \frac{k\rho g}{\mu} \quad (3.19)$$

where k is permeability [m²], ρ is density [kg/m³], g is gravity [m/s²] and μ is viscosity of the fluid [kg/ms]. Table 3.1 presents the correspondence between the variables and relations of water flow (Darcy's law) and electric current flow (Ohm's law).

Table 3.1: Correspondence between electric current flow and water flow.

	Darcy's law: $q = -K\nabla h$	Ohm's law: $J = -\sigma\nabla\phi$
Flux of:	Water q [m/s]	Charge J [A/m ²]
Potential:	Head h [m]	Voltage ϕ [V]
Medium property:	Hydraulic conductivity K [m/s]	Electrical conductivity σ [1/ Ω m]

The similarities between these two equations imply that it should be possible to use flow simulator like TOUGH2 to solve electric field due to flow of electric current. In that case the pressure results from TOUGH2 would correspond to the electric voltage, the current density to the flow of water and the electrical conductivity would correspond to the hydraulic conductivity, i.e.

$$\sigma = \frac{k\rho g}{\mu} \quad (3.20)$$

TOUGH2 and the previously described resistivity model use different solving techniques which could cause some difference in the results between the two programs. TOUGH2 is an integrated finite difference program so it calculates the average value of the solution

over some finite volume of space in stead of calculating the solutions at points in a finite element mesh like done in the resistivity model.

In order to investigate the possibility of using TOUGH2 to solve electric potential a flow simulation was performed using TOUGH2 on a grid with dimensions $160 \times 160 \times 10 \text{ m}^3$. The reservoir was modeled with porosity 0.4, density 2600 kg/m^3 , permeability 10^5 md (10^{-10} m^2) and no-flow boundary conditions. Water was injected at 100 kg/s in one corner of the reservoir and produced at 100 kg/s in the opposite corner. The initial pressure was set to $9.6 \times 10^5 \text{ Pa}$, temperature to 150°C and single-phase, isothermal conditions were used. Figure 3.6 shows pressure distribution when steady-state condition had been reached.

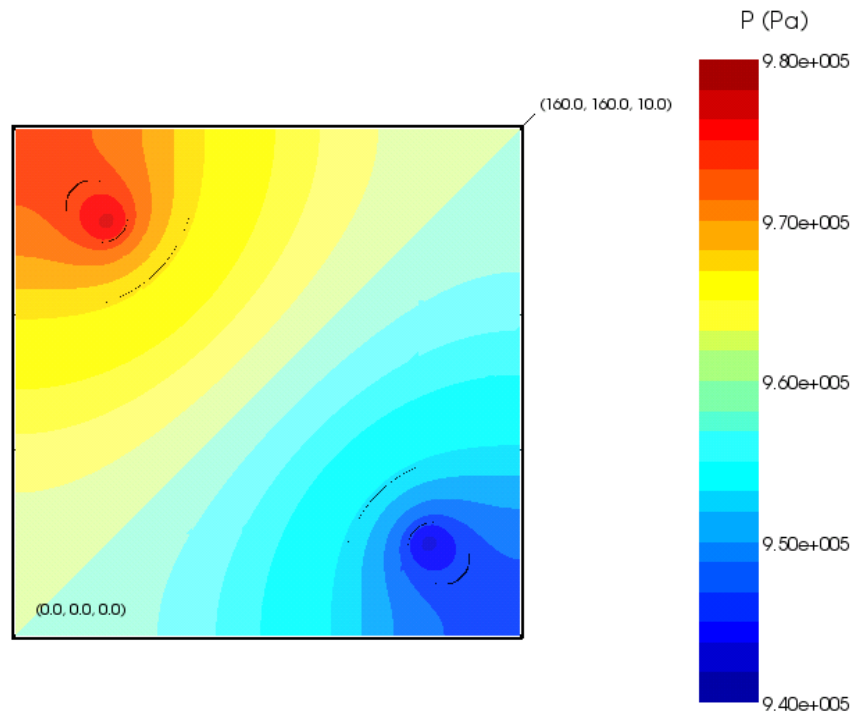


Figure 3.6: Pressure distribution for a homogeneous reservoir.

Next, the possibility of using the resistivity program previously described to solve the same problem was explored. The resistivity was defined as $71.583 \text{ } \Omega\text{m}$ using Equation 3.20, where the viscosity was defined at $9.6 \cdot 10^5 \text{ Pa}$ and 150°C , i.e. $\mu = 1.8258 \cdot 10^{-4}$. Electric current of 100 A was injected in the upper left corner and -100 A in the lower right corner. The results can be seen in Figure 3.7.

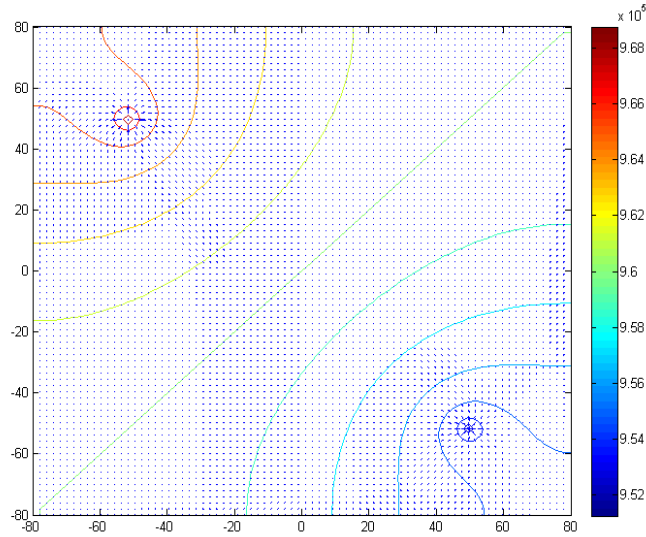


Figure 3.7: Electric potential [V] for a homogeneous reservoir.

The pressure distribution in Figure 3.6 is similar to the voltage distribution in Figure 3.7 but the values are though not the same. The maximum and minimum pressures in Figure 3.6 are 9.800×10^5 Pa and 9.399×10^5 Pa while the maximum and minimum voltage in Figure 3.7 are 9.687×10^5 V and 9.513×10^5 V. In the flow simulation the viscosity changes with pressure but in the resistivity model the conductivity value is defined as a constant, calculated using the viscosity at the mean pressure. The same electrical simulation was performed using the viscosity at the maximum and minimum pressures but the changes in results were negligible.

Another case was considered where the reservoir is inhomogeneous. A few blocks in the middle of the reservoir (green) were modeled with permeability 2.3861×10^{-10} m², i.e. hydraulic conductivity 0.333 m/s and electrical resistivity 30 Ωm, see Figure 3.8.

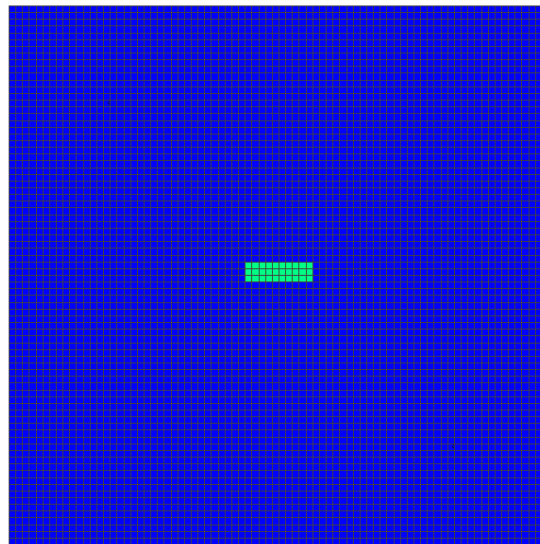


Figure 3.8: Inhomogeneous reservoir.

The maximum and minimum values for the field using these two different programs are shown in Table 3.2.

Table 3.2: Results from TOUGH2 and resistivity model compared.

	TOUGH2	Resistivity model
Maximum	9.7997×10^5 Pa	9.6870×10^5 V
Minimum	9.4002×10^5 Pa	9.5130×10^5 V

As for the homogeneous field, the pressure for the inhomogeneous field calculated using TOUGH2 simulator is different from the electric potential calculated using the resistivity model. The variables and the relations between the two programs are currently being studied further to find a way to use TOUGH2 flow simulator successfully to solve the electric field and thereby making the simulations faster and more efficient, as well as enabling the use of nonrectangular elements.

3.6 FUTURE WORK

The results showed an attempt to use TOUGH2 flow simulator to solve the electric potential. The results from a previously developed resistivity model were different from the TOUGH2 results, so next step involves studying further the analogy between the two programs to find a way to make TOUGH2 solve the equations describing electrical current flow instead of fluid flow. The potential difference could then be calculated for more complicated and realistic fracture patterns using nonrectangular elements.

Other future goals are to use tracer concentration simulations and electrical potential calculations from TOUGH2 with inverse modeling to estimate the dimensions and topology of a fracture network. The objective is to develop a method which can be used to find where fractures are located and the character of their distribution.

In inverse modeling the results of actual observations are used to infer the values of the parameters characterizing the system under investigation. In this study, the output parameters would be the potential differences between wells as a function of time and the input parameters would include the dimensions and orientations of the fractures between the wells. The objective function measures the difference between the model calculation (the calculated voltage difference between the wells) and the observed data (measured potential field between actual wells), as illustrated in Figure 3.9, and a minimization algorithm proposes new parameter sets that improve the match iteratively.

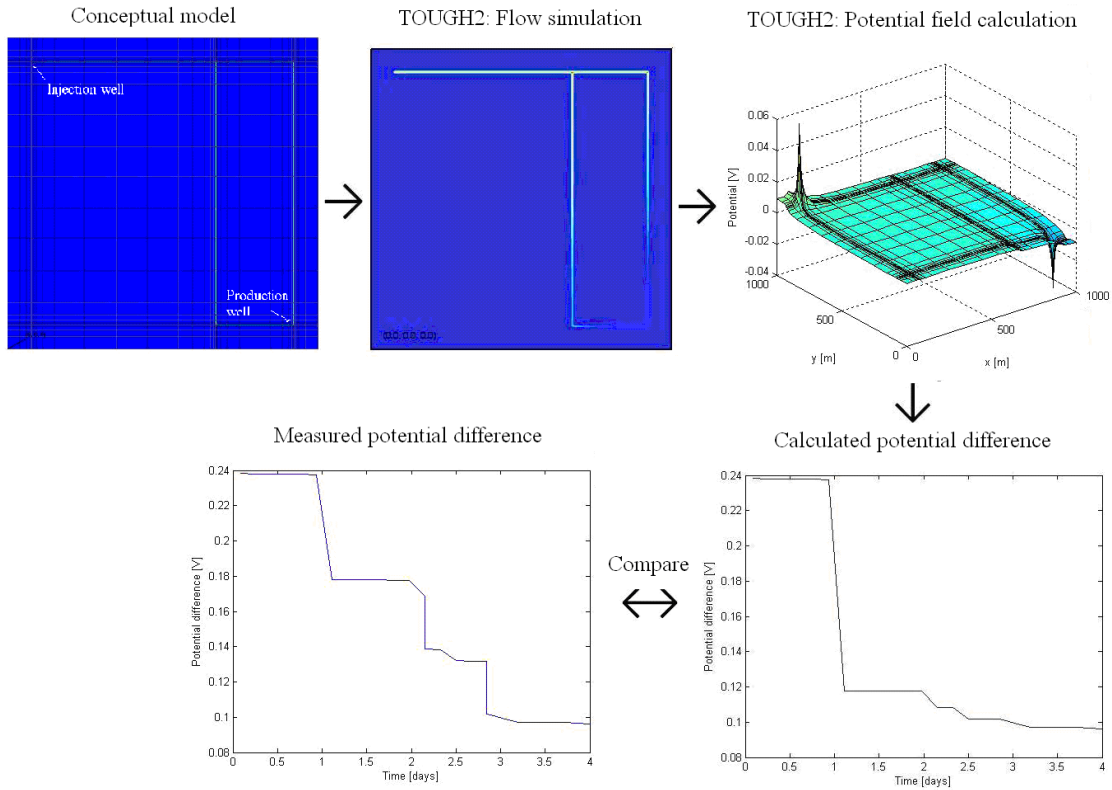


Figure 3.9: The inverse problem; the calculated potential difference is compared to the measured potential difference and the inverse problem solved to characterize fracture patterns.

The possibility of using fewer wells and different well arrangements will be studied to estimate the minimum number of measurement locations necessary to solve the problem.

4. FRACTURE APERTURE DETERMINATION USING THERMAL AND TRACER DATA

This research project is being conducted by Research Associate Carla Kathryn Co and Professor Roland Horne. The overall objective of this study is to develop a methodology to estimate fracture dimensions. Our current focus is on utilizing thermal breakthrough and tracer return data to determine effective fracture apertures.

4.1 SUMMARY

This study aims to determine an effective fracture aperture using tracer concentration and thermal breakthrough profiles. A single fracture was used to represent the connectivity between injection and production well pairs. An analytical model derived by Gringarten and Sauty (1975) was used to estimate the fracture aperture from thermal breakthrough time and mean tracer arrival time. Estimated effective fracture aperture values were recalculated and now vary from 1.7 cm to 11.8 cm.

To further understand the current knowledge of fractures in geothermal rocks, a literature review was undertaken this quarter. Fields included in this study were Desert Peak, Nevada and Wairakei, New Zealand. Fracture properties were determined from acoustic imaging techniques. Feed zone locations identified from pressure, temperature, and spinner (PTS) data were then correlated to these properties. Results showed that feed zone locations correspond to depths with higher apertures. Fracture density, however, is not relevant to fluid entry zones.

4.2 INTRODUCTION

Fracture aperture is an important parameter in geothermal reservoirs. Aperture influences transport and thermal behavior of the reservoir, both in EGS and in conventional hydrothermal systems. An important application is the determination of the degree of interwell connectivity. Of critical importance is the prevention of thermal breakthrough from injection wells to production wells. During the 1980s, several attempts were made to estimate fracture aperture by matching tracer test data, however these were unsuccessful because the parameter estimation problem has multiple degrees of freedom, which makes it difficult to separate fracture aperture from other unknown reservoir parameters. To constrain the degrees of freedom, thermal response data could be used. This was proposed in the 1980s also, however at the time no data existed that provided both tracer and thermal responses. Now that several EGS and fractured reservoirs have been monitored to provide these data, the possibility now exists to estimate fracture aperture in those fields. In this project, a single fracture model was used to describe the connectivity of an injection and production well pair. Tracer and thermal data were used to estimate the fracture width for this simplified model.

The main objective of the work last quarter was to determine whether it would be feasible to derive reasonable estimates for the fracture aperture using both thermal and tracer test results. A secondary objective was to document existing analytical models and field data

available in literature. Furthermore, the fracture width values calculated were compared to those derived from other datasets to check for consistency.

This quarter, aperture values were reevaluated to account for the actual temperature ratio and to correct miscalculations from last quarter. In addition, studies on fracture characterization using acoustic imaging were reviewed to develop a better understanding of feed zone related fractures. Several attempts to simulate a single fracture between wells were made but were not completed yet.

4.3 METHODOLOGY

4.3.1 Analytical Model

Gringarten and Sauty (1975) derived a solution that can be used for unsteady-state one-dimensional heat transfer through a fracture. The solution was similar to that for a porous medium, derived by Lauwerier (1955). The solution assumes a thin, uniform reservoir with an adiabatic boundary. Heat is transferred by conduction from the rock layers and the entering fluid. Since no mixing is assumed, the result is a stream-like channel flow.

Horne (1996) derived the resulting analytical solution for this model as Equation 4.1 where t_c is the tracer front arrival time, t_{th} is the thermal breakthrough time, and b is the fracture aperture. On the left hand side of Equation 4.1 is the relative temperature ratio T_{ratio} . Here, T_o is the original reservoir temperature, T_w is the reservoir temperature at x , and T_{inj} is the injected fluid temperature. Thus, the fracture aperture can be determined using the thermal and tracer breakthrough data. Knowledge of the fracture aperture can then be used to predict temperature drawdown in producing wells.

$$T_{ratio} = \frac{T_o - T_w}{T_o - T_{inj}} = \operatorname{erfc} \left\{ \left[\frac{(\rho_w C_w)^2 \left(\frac{b}{t_c}\right)^2 (t_{th} - t_c)}{K_r \rho_r C_r} \right]^{-\frac{1}{2}} \right\} \quad (4.1)$$

$$b = \left\{ \left(\operatorname{erfc}^{-1} \left[\frac{T_o - T_w}{T_o - T_{inj}} \right] \right)^{-2} \frac{t_c^2 K_r \rho_r C_r}{(t_{th} - t_c) (\rho_w C_w)^2} \right\}^{1/2} \quad (4.2)$$

These are the analytical expressions used to model a single fracture connection between an injector and producer well pair. Equation 4.2 calculates the effective fracture aperture from the thermal arrival time t_{th} ; tracer front arrival time t_c ; and relative temperature ratio T_{ratio} .

4.3.2 Available field data

Results from tracer tests in EGS and conventional fractured geothermal reservoirs have been reported frequently in the literature. However, thermal breakthrough data are not as widely published. For EGS fields, thermal data were obtained usually from long-term circulation tests, as for example in Hijiori, Matsunaga et al. (2002) and Matsunaga et al. (2005). Historic silica geothermometer data were used from Palinpinon field which is a conventional liquid-dominated reservoir, Maturgo et al. (2010). Matsukawa is a conventional vapor-dominated field, Fukuda et al. (2006). Table 4.1 provides a summary of the field data used in this study. The thermal breakthrough time t_{th} here corresponds to the time it takes to reach the T_{ratio} listed in Table 4.3.

Table 4.1: Thermal and tracer breakthrough times from field data.

Field	Injector	Producer	t_c	t_{th}	Source
			days	days	
Hijiori	HDR-1	HDR-2A	1	230	Matsunaga et al. (2002)
	HDR-1	HDR-3	4	293	Matsunaga et al. (2005)
Palinpinon	NJ2RD	NJ5D	15	1095 ¹	Maturgo et al. (2010)
	SG2RD	NJ3D	28	657	
Matsukawa	M-6	M-8	1.5	146	Fukuda et al. (2006)

4.4 PRELIMINARY CALCULATIONS AND RESULTS

As described in the previous section, fracture aperture can be estimated directly from the thermal and tracer breakthrough time. Assumptions for the values of the other parameters are listed in Table 4.2. These were the values assigned to these properties in the estimation of fracture aperture. Actual temperature ratios for the injector-producer pairs derived from long term circulation test results are shown in Table 4.3. Estimated fracture aperture values are given in the same table.

To determine the relative temperature for M-6 and M-8 in Matsukawa, a 60°C injection temperature was assumed. Estimates of effective fracture aperture b vary from 1.7 cm to 11.8 cm. Though the HDR-1 and HDR-2A well pair in Hijiori exhibited the shortest mean tracer arrival time, it had the lowest calculated effective aperture value because of the long thermal breakthrough time. This observation demonstrates the value of using both tracer and thermal results to constrain the effective aperture. Using this analytical solution also provides an alternative method to characterize the flow path between wells.

Results from finite element heat and mass transfer modeling (FEHM) of the Hijiori field demonstrates fracture aperture values of about 2 mm (Tenma et al., 2005). This is significantly lower than the recalculated aperture values. Further investigation of results

¹ Assumed that injection in NJ2RD started in 1998 or 1 year before the start of drawdown in NJ5D based on the discussion of cooling rates by Maturgo et al. (2010)

from aperture estimates from numerical modeling will be undertaken. However, effective fracture aperture derived from acoustic imaging logs show a range of values consistent with those calculated. The next section will describe these studies in detail.

Table 4.2: Assumptions used in calculations.

Rock thermal conductivity	K_r	2	W/m-C
Rock density	ρ_r	2200	kg/m ³
Water density	ρ_w	900	kg/m ³
Rock heat capacity	C_r	0.712	kJ/kg-C
Water heat capacity	C_w	4.342	kJ/kg-C

Table 4.3: Relative temperature ratios and calculated fracture aperture from thermal and tracer breakthrough times.

Field	Injector	Producer	T_{ratio}	Calculated b
				cm
Hijiori	HDR-1	HDR-2A	0.46	1.7
	HDR-1	HDR-3	0.14	3.0
Palinpinon	NJ2RD	NJ5D	0.17	6.2
	SG2RD	NJ3D	0.07	11.8
Matsukawa	M-6	M-8	0.29 ²	2.2

4.5 REVIEW OF RELATED LITERATURE

4.5.1 Acoustic Imaging

Characterization of fluid flow in fractures is an important area of study in geothermal reservoir engineering. Overall permeability in these reservoirs is fault-dominated (Massart, 2010). Relevant fracture parameters to fluid flow are: orientation, aperture, extension, and density. These parameters influence transport and thermal behavior of the reservoir, both in enhanced geothermal systems (EGS) and in conventional hydrothermal systems. Recent advances in borehole imaging technology have made it possible to measure fracture properties with greater accuracy.

For the Wairakei geothermal field, McLean and McNamara (2011) used a high temperature acoustic formation imaging tool (AFIT) to collect fracture data. Confidence, azimuth, and amplitude filters were applied to the data prior to analysis. A borehole televiewer (BHTV) similar to AFIT and UBI was also used in the Desert Peak EGS project. In addition, formation microscanner (FMS) image logs were utilized (Devatzes, 2009).

² Assumed an injection temperature of 60°C

Published fracture data from various geothermal fields were collected and analyzed. Data sets examined for this study are fracture aperture and density. These were then compared to locations of feed zones to determine their correlation with fluid flow properties.

Fracture data from the various geothermal fields show consistent correspondence between fracture apertures and feed zone locations for most of the data points. In Wairakei, fracture apertures for the feed zones range from around 10 to 60 centimeters in wells WK-404, WK-318, and WK-407. A similar trend can be observed from the Desert Peak data. Data for well 27-15 had aperture values from 3 to 10 cm at fluid entry zones. Figures 4.1 to 4.4 show the feed zone locations, PTS data, and fracture apertures for various wells in Wairakei and Desert Peak.

There are two possible explanations for this observation. Using a parallel-plate model, fracture permeability is proportional to b^2 , where b is the fracture aperture (Jourde, 2002). Fluid entry, associated to fractures in geothermal reservoirs, occurs at depths with high permeability. Therefore, feed zone locations will be at depths with high apertures. Another rationale is the power-law scaling between joint length and width described by Scholz (2010). Scholz argued that for opening mode in rocks, fracture toughness scales linearly with \sqrt{L} and b scales linearly with L , where L is the length. Therefore, a larger fracture width will correspond to a longer fracture which implies a farther reach for the fluid source.

On the other hand, there appears to be no correlation between fracture density and feed zone depths. Massart et al. (1999) analyzed new data sets from natural faults and extension fractures and validated that it follows power-law scaling in multiple-observational scales. Results from their study show that the power-law scaling applies across six ranges of scale within reasonable uncertainty limits. Zones with higher fracture aperture values will have smaller fracture density. Based on this, regions with higher apertures will have lower fracture density values. Hence, fluid entry points should have lower fracture densities. However, this was not consistently observed in all the data. The lack of inverse correspondence between fracture density and feed zone location could be due to the binning of data. Tool measurement uncertainties could also cause deviations. Moreover, there is inherent error associated with the inverse scaling of fracture density and aperture.

4.6 FUTURE WORK

Further analysis on this approach to estimating fracture aperture will be undertaken. A review of past studies on fracture characterization using tracer analysis and numerical modeling will be done this quarter. Use of pressure transient analysis for fracture characterization will also be explored.

Previous attempts on the use of numerical simulation to model the effect of fracture aperture on mass and heat transport have been met with challenges. Creating this model and comparing it with the analytical results, however, is still endeavored in the future.

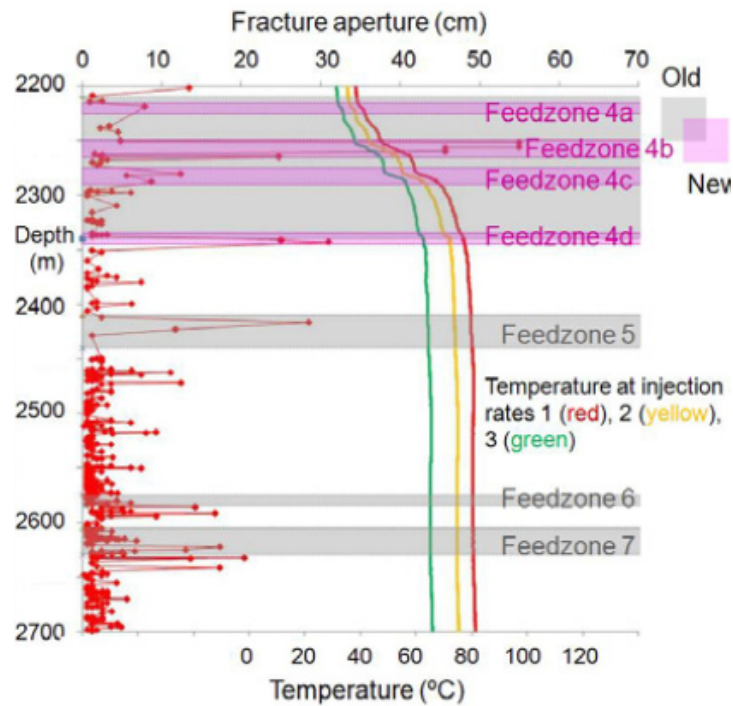


Figure 4.1 Fracture aperture (red) and temperature versus depth for well WK-404 in the Wairakei Geothermal Field (McLean and McNamara, 2011)

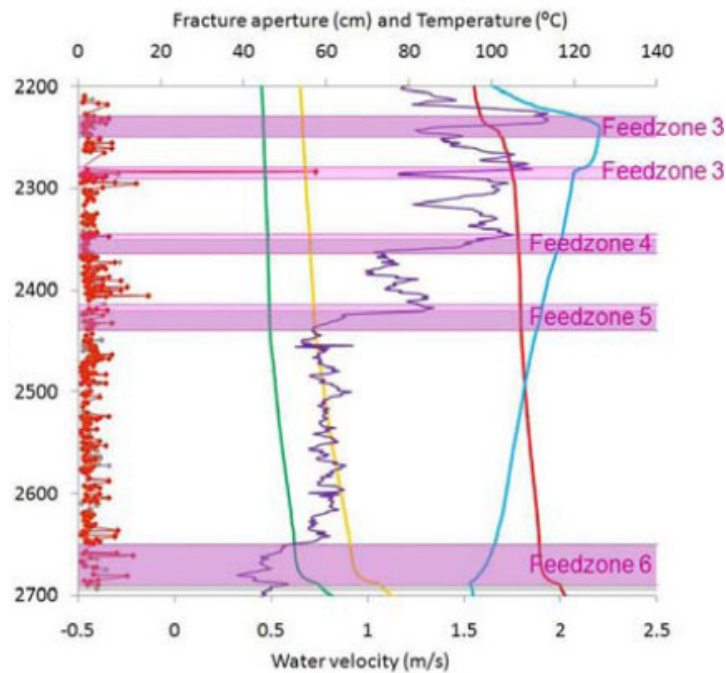


Figure 4.2 Fracture aperture (red), temperature, and spinner velocity (blue) versus depth log for well WK-317 in the Wairakei Geothermal Field (McLean and McNamara, 2011)

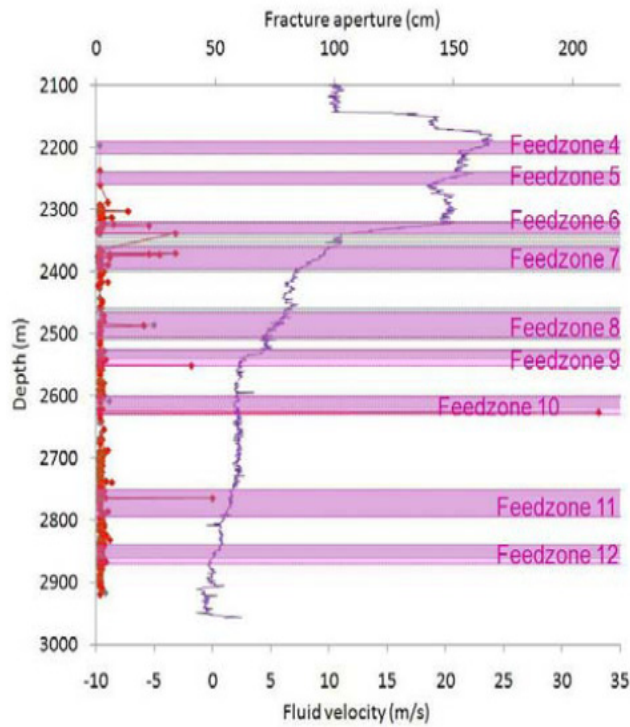


Figure 4.3 Aperture (red) and spinner velocity (blue) versus depth log for well WK-407 in the Wairakei Geothermal Field (McLean and McNamara , 2011)

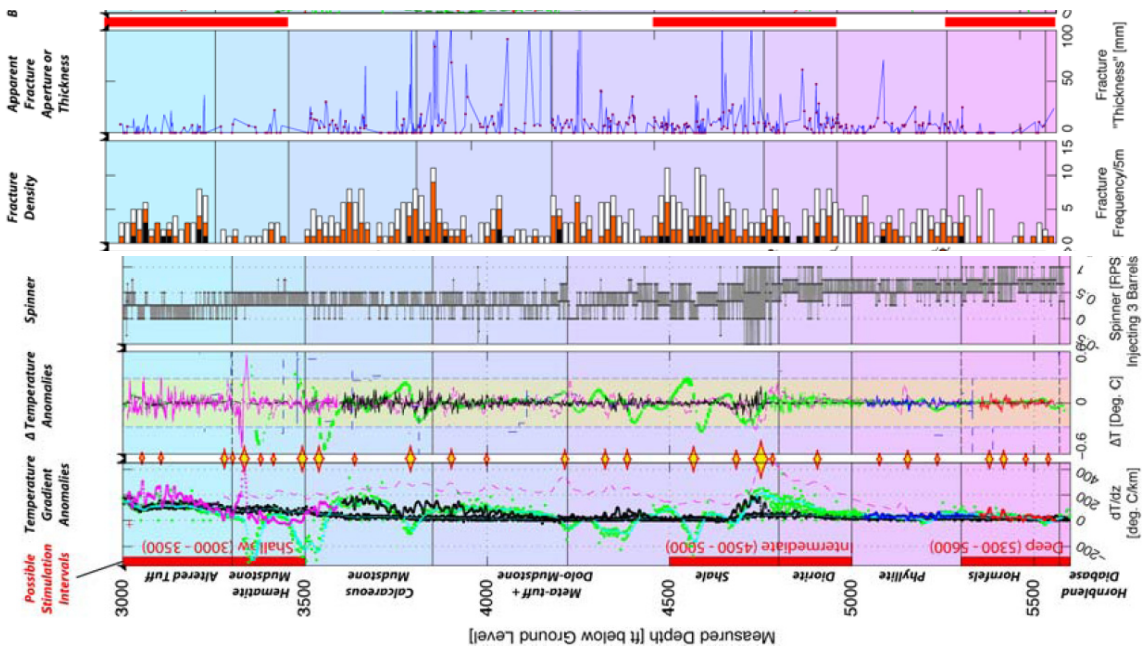


Figure 4.4 Well Log data for well 27-15 in the Desert Peak Geothermal Field, Nevada. Yellow diamonds indicate feed zones derived from temperature anomalies and spinner velocities (Devatzes, 2009)

5. REFERENCES

- Alaskar, M., Ames, M., Horne, R.N., Li, K., Connor, S. and Cui, Y.: “In-situ Multifunction Nanosensors for Fractured Reservoir Characterization,” GRC Annual Meeting, Sacramento, USA, vol. 34 (2010).
- Arnason, K.: Viðnámsmælingar í Jarðhitarannsóknnum á Íslandi, Orkustofnun, Orkuþing (2001).
- Bennett, K. and Horne, R. N., Power Generation Potential from Coproduced Fluids in the Los Angeles Basin, *Geothermal Resources Council*, (2011).
- Bodvarsson, G., and Pruess, K., Thermal effects of reinjection in geothermal reservoirs with major vertical fractures, *Journal of Petroleum Technology*, **36(9)**, (1984), 1567–1578. Society of Petroleum Engineers.
- Chen, H., Li, Z., Wu, Z. and Zhang, Z.: “A novel route to prepare and characterize Sn-Bi nanoparticles,” *Journal of Alloys and Compounds*, 394 (2005), 282-285.
- Crain, E.R.: Crain’s Petrophysical Handbook. Web 17 November 2010. www.spec2000.net
- Devatzes, N.C. and Hickman, S.H.: “Fractures, stress, and fluid flow prior to stimulation of well 27-15, Desert Peak, Nevada, EGS project,” *Proceedings 34th workshop on Geothermal Reservoir Engineering*, Stanford University. 2009.
- Devatzes, N.C. and Hickman, S.H.: “In-situ stress and fracture characterization for planning of an EGS stimulation in the Desert Peak Geothermal Field, Nevada,” *Proceedings 35th workshop on Geothermal Reservoir Engineering*, Stanford University. 2010.
- Dey, A. and Morrison, H.F.: Resistivity Modeling for Arbitrarily Shaped Two-Dimensional Structures, *Geophysical Prospecting* 27, I06-I36, University of California, Berkeley, CA (1979).
- Fukuda, D., Akatsuka, T., and Sarudate, M: “Characterization of inter-well connectivity using alcohol tracer and steam geochemistry in the Matsukawa vapor-dominated geothermal field, Northeast Japan,” *GRC Transactions*. 2006, 797-801.
- Gentier, S., Rachez, X., Ngoc, T., Dung, T., Peter-Borie, M., and Souque, C., 3D flow modelling of the medium-term circulation test performed in the deep geothermal site of Soultz-sous-Forêts (France), *World Geothermal Congress*, (2010), International Geothermal Association.
- Gringarten, A.C. and Sauty, J. P.: “A theoretical study of heat extraction from aquifers with uniform regional flow,” *Journal of Geophysical Research*. 1975, 4956-122.
- Gringarten, A. C., and Witherspoon, P., Theory of heat extraction from fractured hot dry rock. *Journal of Geophysical Research*, **80(8)**, (1975), 1120-1124.

- Holder, D.S.: Electrical Impedance Tomography: Methods, History and Applications, IOP, UK (2004).
- Horne, R.N.: "Reservoir Engineering of Reinjection," Course Notes. Stanford University, 1996.
- Jourde, H. et.al.: "Computing permeability of fault zones in eolian sandstone from outcrop measurements," *American Association of Petroleum Geologists Bulletin*. 2002.
- Kocabas, I., Geothermal reservoir characterization via thermal injection backflow and interwell tracer testing. *Geothermics*, **34(1)**, (2005), 27-46.
- Lauwerier, H. A., The transport of heat in an oil layer caused by the injection of hot fluid. *Applied Scientific Research*, **5(2)**, (1955) 145-150.
- Lee, K. H., Ortega, A., Jafroodi, N., Ershaghi, I., SPE132625: A Multivariate Autoregressive Model for Characterizing Producer Producer Relationships in Waterfloods from Injection/Production Rate Fluctuations, *SPE Western Regional Meeting*, (2010).
- Lovekin, J. and Horne, R. N., Optimization of injection scheduling in geothermal fields, *DOE Research and Development for the Geothermal Marketplace, Proceedings of the Geothermal Program Review VII*, (1989), pp. 45-52.
- Marrett, R. et al.: "Extent of power-law scaling for natural fractures in rock," *Geology*. 1999.
- Massart, B., Paillet, M., Henrion, V., Sausse, J., Dezayes, C., Genter, A., Fracture Characterization and Stochastic Modeling of the Granitic Basement in the HDR Soultz Project (France). *World Geothermal Congress*, (2010), International Geothermal Association.
- Matsunaga, I., Yanagisawa, N., Sugita, H., Tao, H.: "Reservoir monitoring by tracer testing during a long term circulation test at the Hijiori HDR site," *Proceedings, Twenty-Seventh Workshop on Geothermal Reservoir Engineering*, Stanford University. 2002.
- Matsunaga, I., Yanagisawa, N., Sugita, H., Tao, H.: "Tracer tests for evaluation of flow in a multi-well and dual fracture system at the Hijiori HDR test site," *Proceedings, World Geothermal Congress*. 2005.
- Maturgo, O.O., Sanchez, D. R., and Barroca, G.B.: "Tracer test using naphthalene disulfonates in Southern Negros Geothermal Production Field, Philippines," *Proceedings, World Geothermal Congress*. 2010.
- McLean, K. and McNamara, D.: "Fractures interpreted from acoustic formation imaging technology: correlation to permeability," *Proceedings, 36th workshop on Geothermal Reservoir Engineering*, Stanford University. 2011.
- Mufti, I.R.: Finite-Difference Resistivity Modeling for Arbitrarily Shaped Two-Dimensional Structures, *Geophysics*, **41**, (1976), 62-78.

- Place, J., Garzic, E. L. E., Geraud, Y., Diraison, M., and Sausse, J., Characterization of the Structural Control on Fluid Flow Paths in Fractured Granites. *Thirty-Sixth Workshop on Geothermal Reservoir Engineering*, (2011), Stanford University.
- Pritchett, J.W.: Finding Hidden Geothermal Resources in the Basin and Range Using Electrical Survey Techniques. A Computational Feasibility Study, report INEEL/EXT-04-02539 (2004).
- Pruess, K. and Bodvarsson, G. S.: "Thermal effects of reinjection in geothermal reservoirs with major vertical fractures," *Journal of Petroleum Technology*. 1984, 1567-1578.
- Scholz, C.H.: "A note on the scaling relations for opening mode fractures in rock," *Journal of Structural Geology*. 2010.
- Shook, G. M., Predicting thermal breakthrough in heterogeneous media from tracer tests. *Geothermics*, **30(6)**, (2001).
- Shook, G. M., A simple, fast method of estimating fractured reservoir geometry from tracer tests. *Geothermal Resources Council*, (2003).
- Shook, G. M., Estimating Fracture Surface Areas from Tracer Tests: Mathematical Formulation. *Geothermal Resources Council*, (2004).
- Singha, K. and Gorelick, S.M. Saline Tracer Visualized with Three-dimensional Electrical Resistivity Tomography: Field-scale Spatial Moment Analysis. *Water Resources Research*, **41** (2005), W05023.
- Slater, L., Binley, A.M., Daily, W. and Johnson, R. Cross-hole Electrical Imaging of a Controlled Saline Tracer Injection. *Journal of Applied Geophysics*, **44**, (2000), 85-102.
- Spencer, R.L. and Ware, M.: Computational Physics 430, Partial Differential Equations, Department of Physics and Astronomy, Brigham Young University (2009).
- Stacey, R.W., Li, K. and Horne, R.N.: Electrical Impedance Tomography (EIT) Method for Saturation Determination, *Proceedings*, 31st Workshop on Geothermal Reservoir Engineering, Stanford University, Stanford, CA (2006).
- Tenma, N., Yamaguchi, T., and Zyvoloski, G.: Variation of the characteristics of the shallow reservoir at the Hijiori test site between 90-days circulation test and long-term circulation test using FEHM code." *Proceedings*, World Geothermal Congress. 2005.
- Tester, J., Anderson, B., Batchelor, A., Blackwell, D., DiPippo, R., Drake, E., et al., The future of geothermal energy: Impact of Enhanced Geothermal Systems on the United States in the 21st Century, (2006), Massachusetts Institute of Technology.
- The MathWorks: Partial Differential Equation Toolbox 1, The MathWorks™, Inc. (2003).

- Wang, P. and Horne, R.N.: Integrating Resistivity Data with Production Data for Improved Reservoir Modeling, SPE 59425, SPE Asia Pacific Conference, Yokohama, Japan (2000).
- Wu, X., Pope, G., Shook, G. M., and Srinivasan, S., Prediction of enthalpy production from fractured geothermal reservoirs using partitioning tracers. *International Journal of Heat and Mass Transfer*, **51(5-6)**, (2008), 1453-1466.